Origin of Ultra-high Energy Cosmic Rays: Some Perspectives of a Theorist

1. Cosmic Rays and the non-thermal Universe: Some general considerations
2. Ultra-high energy cosmic rays: theoretical challenges, multi-messenger aspects
3. Anisotropies and 3-dimensional propagation

Deutsche Forschungsgemeinschaft

PROJEKTTRÄGER FÜR DAS Bundesministerium für Bildung und Forschung

Günter Sigl
II. Institut theoretische Physik, Universität Hamburg
Hillas Symposium, Heidelberg, 10.12-12.12.2018

Universität Hamburg
DER FORSCHUNG | DER LEHRE | DER BILDUNG

The All Particle Cosmic Ray Spectrum

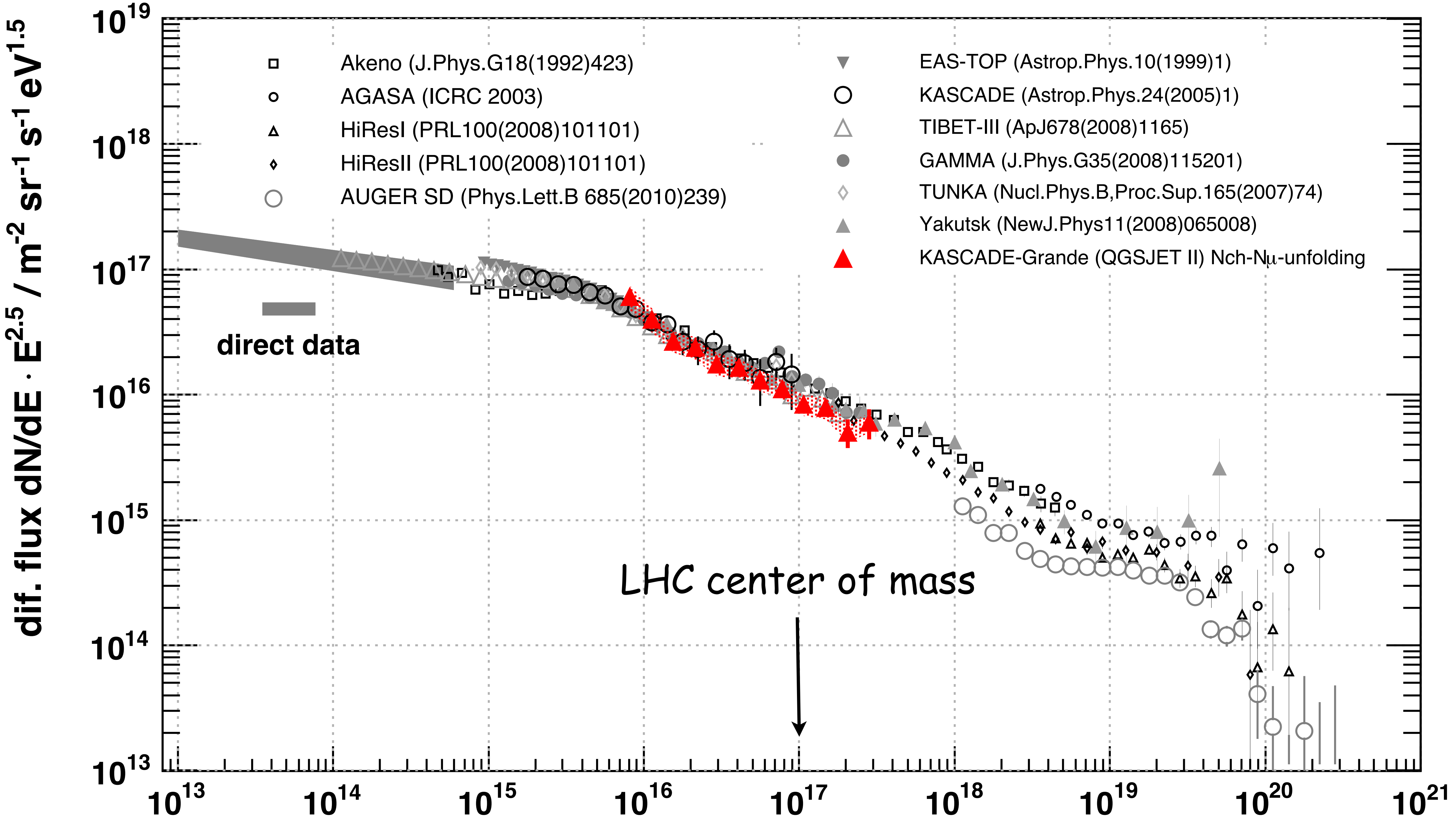

KASCADE-Grande collaboration, arXiv:1111.5436

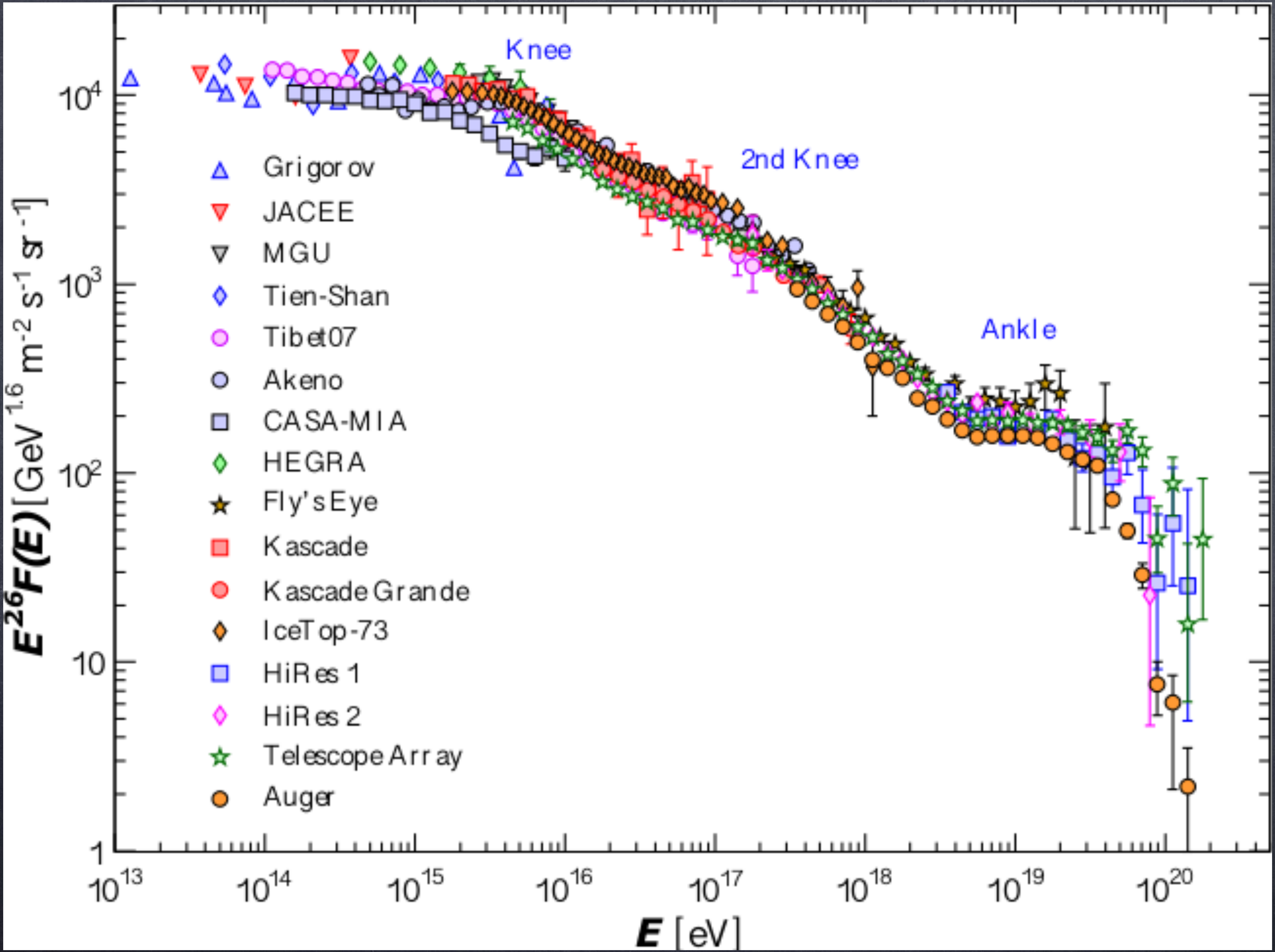

Knee
2nd Knee
Ankle
Grigorov
JACEE
MGU
Tien-Shan
Tibet07
Akeno
CASA-MIA
HEGRA
Fly's Eye
Kascade
Kascade Grande
IceTop-73
HiRes 1
HiRes 2
Telescope Array
Auger
$E^{2.6}F(E)$ [GeV$^{1.6}$ m^{-2} s^{-1} sr^{-1}]
E [eV]
1
10
10^2
10^3
10^4
10^{13}
10^{14}
10^{15}
10^{16}
10^{17}
10^{18}
10^{19}
10^{20}

Pierre Auger Spectra

Auger exposure = 50000 km^2 sr yr, 102901 events above 3×10^{18} eV until end 2014

Pierre Auger Collaboration, PRL 101, 061101 (2008)
and Phys.Lett.B 685 (2010) 239
ICRC 2015, arXiv:1509.03732

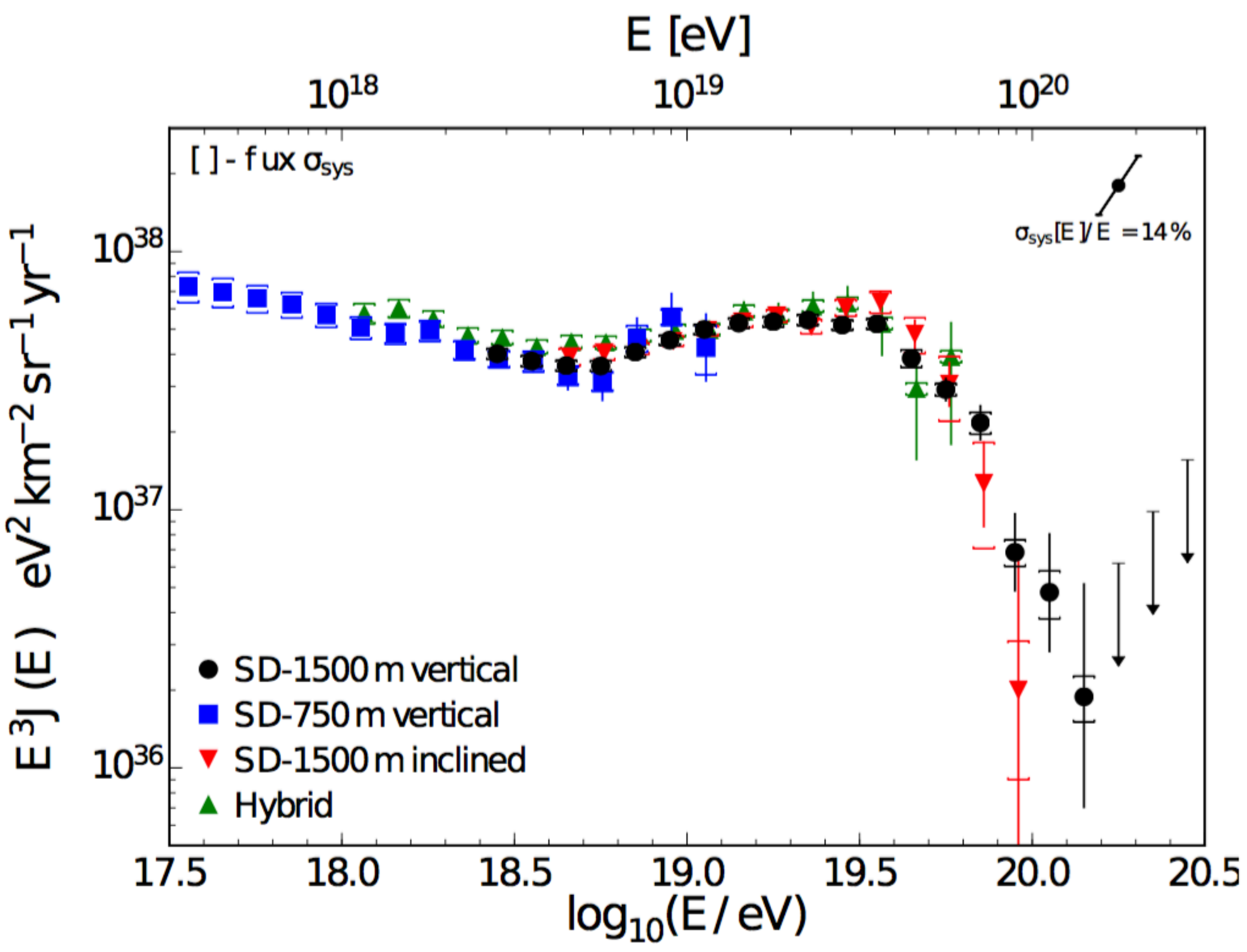

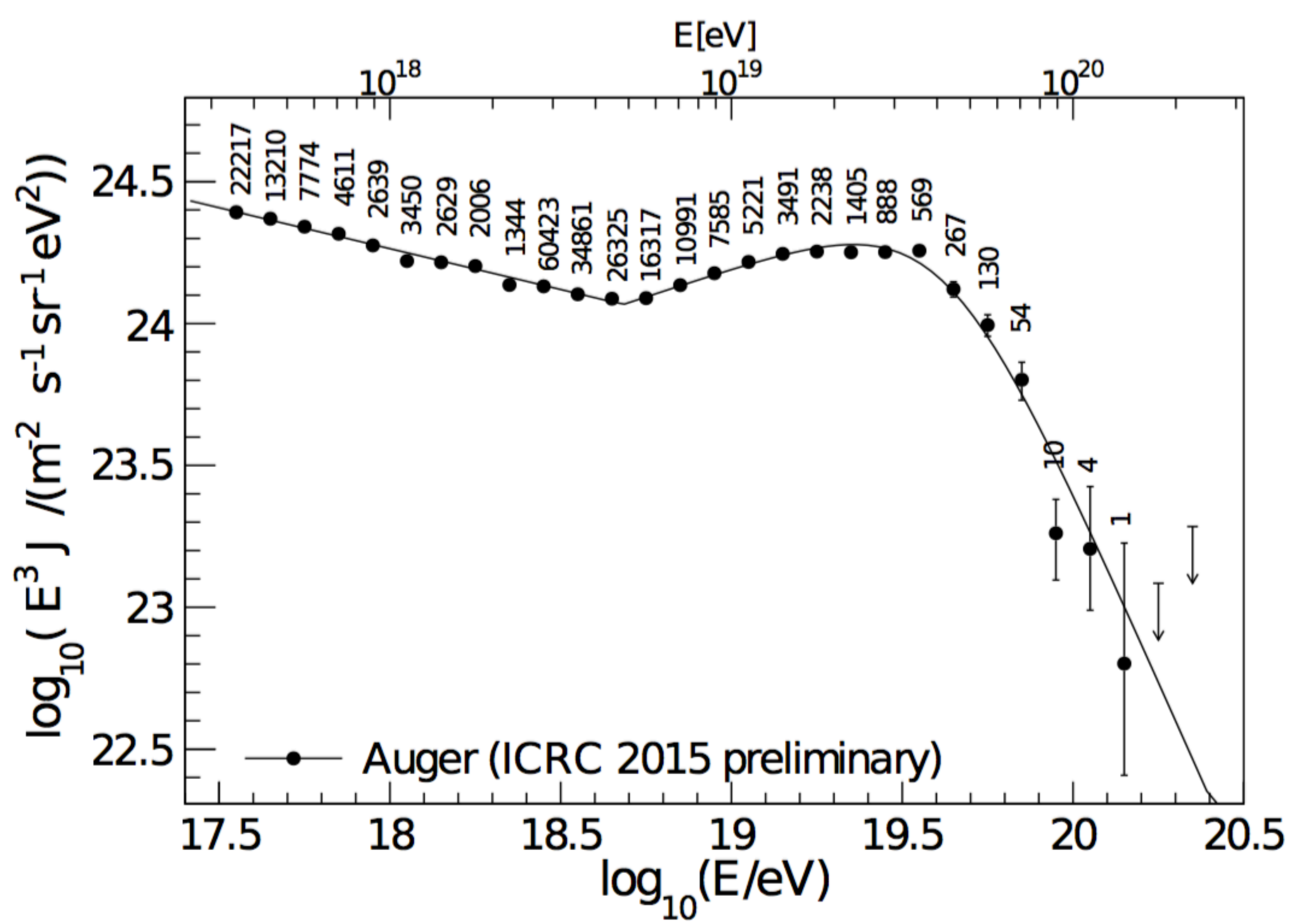

Cosmic Rays and the Non-Thermal Universe: General Considerations

(based on discussions with Jörg Rachen)
Cosmic ray energy density dominated by extragalactic flux,

$$\rho_{\rm CR} \sim \frac{4\pi}{c_0}\int d\ln E E^2 j(E) \geq 4\pi E_{\rm eg}^2 j(E_{\rm eg}) \sim 5.9\times 10^{54}\,{\rm erg\,Mpc}^{-3}\,, \quad E_{\rm eg}\sim 10^{18}\,{\rm eV}\,,$$

because $E^2 j(E)$ decreases with energy, so is dominated by smallest energy dominated by extragalactic flux
For energy loss time $T_{loss}(E)$ this corresponds to a power

$$\frac{L_{\rm CR}}{V} \sim \frac{4\pi}{c_0}\int d\ln E \frac{E^2 j(E)}{T_{\rm loss}(E)} \sim 10\,\frac{\rho_{\rm CR}}{t_0} \sim 4.3\times 10^{45}\,{\rm erg\,Mpc}^{-3}{\rm y}^{-1}\,,$$

because $E^2 j(E)/T_{loss}(E)$ only weakly depends on energy and $T_{loss}(E)$ becomes comparable to the Hubble rate $H_0 \sim 1/t_0$ at $E \sim E_{eg}$.
Now compare this with the thermal and non-thermal power in the Universe.

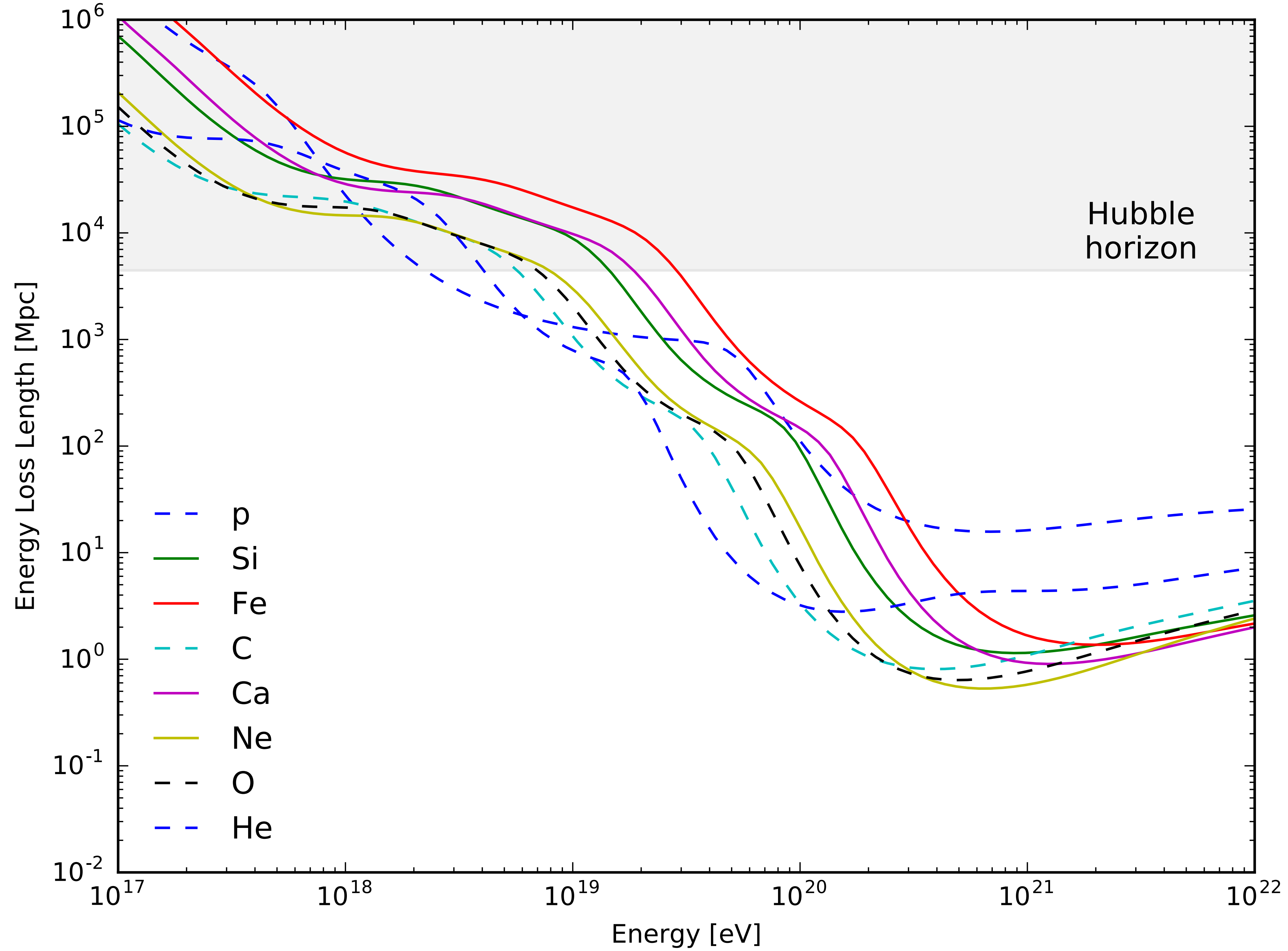

G. Sigl, book “Astroparticle Physics: Theory and Phenomenology”, Atlantis Press/Springer 2016

If a fraction $f_s \sim 5\%$ of the baryonic matter has been cycled through stars until today of which a nuclear binding energy fraction $f_n \sim 10^{-3}$ is released in stellar fusion then the thermal energy density is $\rho_{th} \sim f_s f_n \, \Omega_b \rho_{c,0}$, corresponding to the thermal luminosity

$$\frac{L_{\rm th}}{V} \sim \frac{f_s f_n \Omega_b \rho_{c,0}}{t_0} \sim 4 \times 10^{49} \left(\frac{\Omega_b h^2}{0.022}\right)\left(\frac{f_s}{0.05}\right)\left(\frac{f_n}{10^{-3}}\right) \,\mathrm{erg\,Mpc^{-3}y^{-1}}\,.$$

Similarly, if a fraction f_{nth} of the mass density is transformed into non-thermal energy, its energy density is $\rho_{nth} \sim f_{nth} \, \Omega_m \rho_{c,0}$. We expect f_{nth} to be a fraction of the turbulent energy density per unit mass, thus by the viral theorem $f_{nth} < v_t^2/2 \sim 10^{-6}$ (number typical for largest virialized structures, galaxy clusters). Thus

$$\frac{L_{\rm nth}}{V} \sim \frac{f_{\rm nth} \Omega_m \rho_{c,0}}{t_0} \sim 5.1 \times 10^{48} \left(\frac{\Omega_m h^2}{0.142}\right)\left(\frac{f_{\rm nth}}{10^{-6}}\right) \,\mathrm{erg\,Mpc^{-3}y^{-1}}\,,$$

and a fraction $\sim 10^{-3}$ of the non-thermal power is sufficient to explain L_{CR}.

Estimate of maximal cosmic ray energy in an object of mass M and radius R:

If magnetic field energy is fraction f_B of non-thermal energy,

$$\frac{B^2}{8\pi}\frac{4\pi}{3}R^3 \sim f_B f_{\rm nth} M\,.$$

The virial theorem states that f_{nth} M ~ $U_{pot}/2$ ~ $G_N M^2/R$, implying M ~ f_{nth} R/G_N. Together with equation above this gives

$$B \sim (6f_B)^{1/2} f_{\rm nth}\frac{M_{\rm Pl}}{R}\,,$$

and using the Hillas criterium with v ~ v_t ~ $f_{nth}^{1/2}$ results in

$$E_{\rm max} \leq eZRBv_t \simeq (6f_B)^{1/2} f_{\rm nth}^{3/2} eZM_{\rm Pl} \sim 3\times 10^{18}\, Z\left(\frac{f_{\rm nth}}{10^{-6}}\right)^{3/2}\ {\rm eV}\,.$$

Remarkably this is independent of M and R and comparable to observed maximal energies if highest energy are dominated by heavy composition !

Multi-Messenger Aspects

The „grand unified“ differential neutrino number spectrum

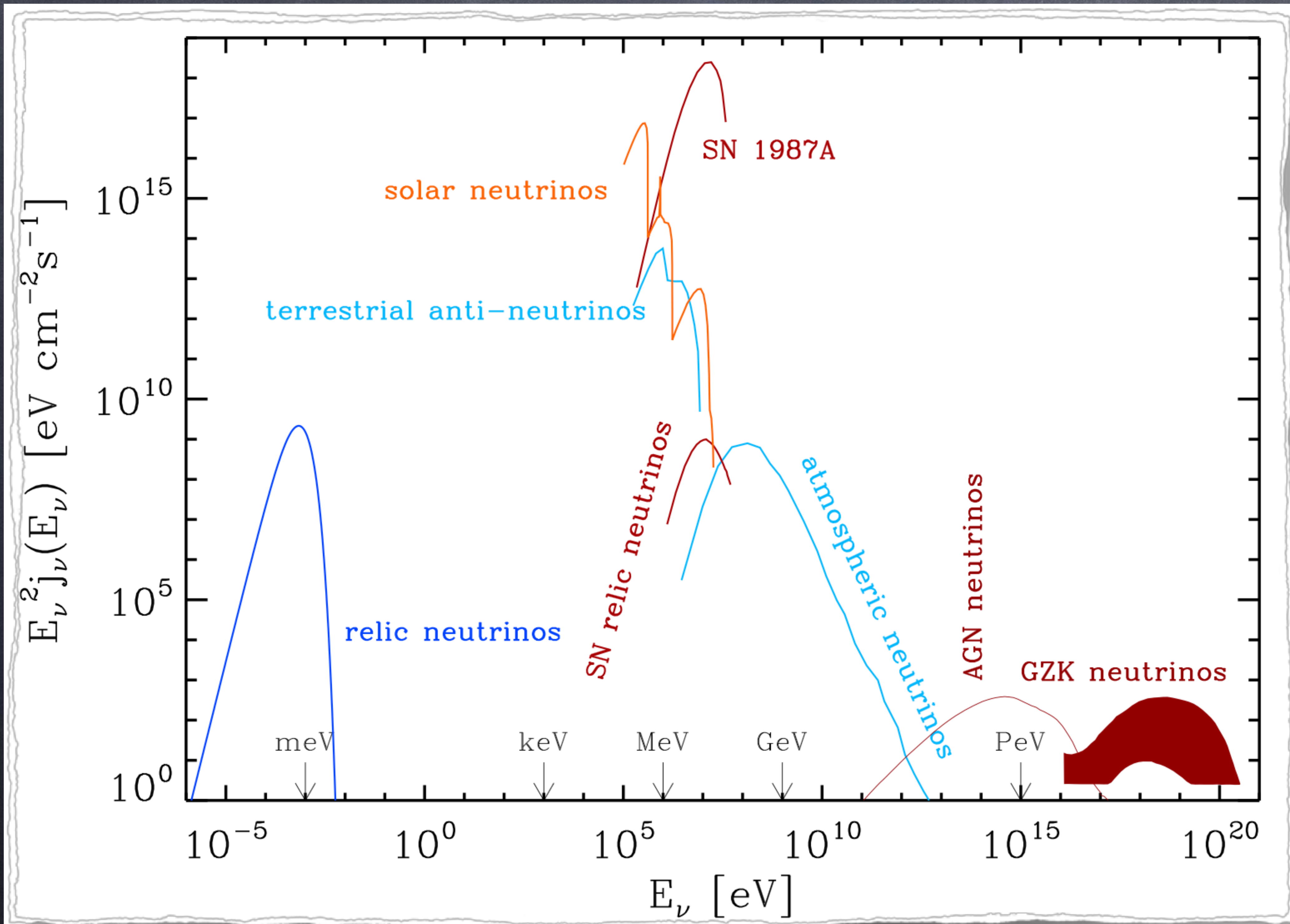

G. Sigl, book
“Astroparticle Physics:
Theory and Phenomenology”,
Atlantis Press/Springer 2016

The universal diffuse photon spectrum

G. Sigl, book
"Astroparticle Physics:
Theory and Phenomenology",
Atlantis Press/Springer 2016

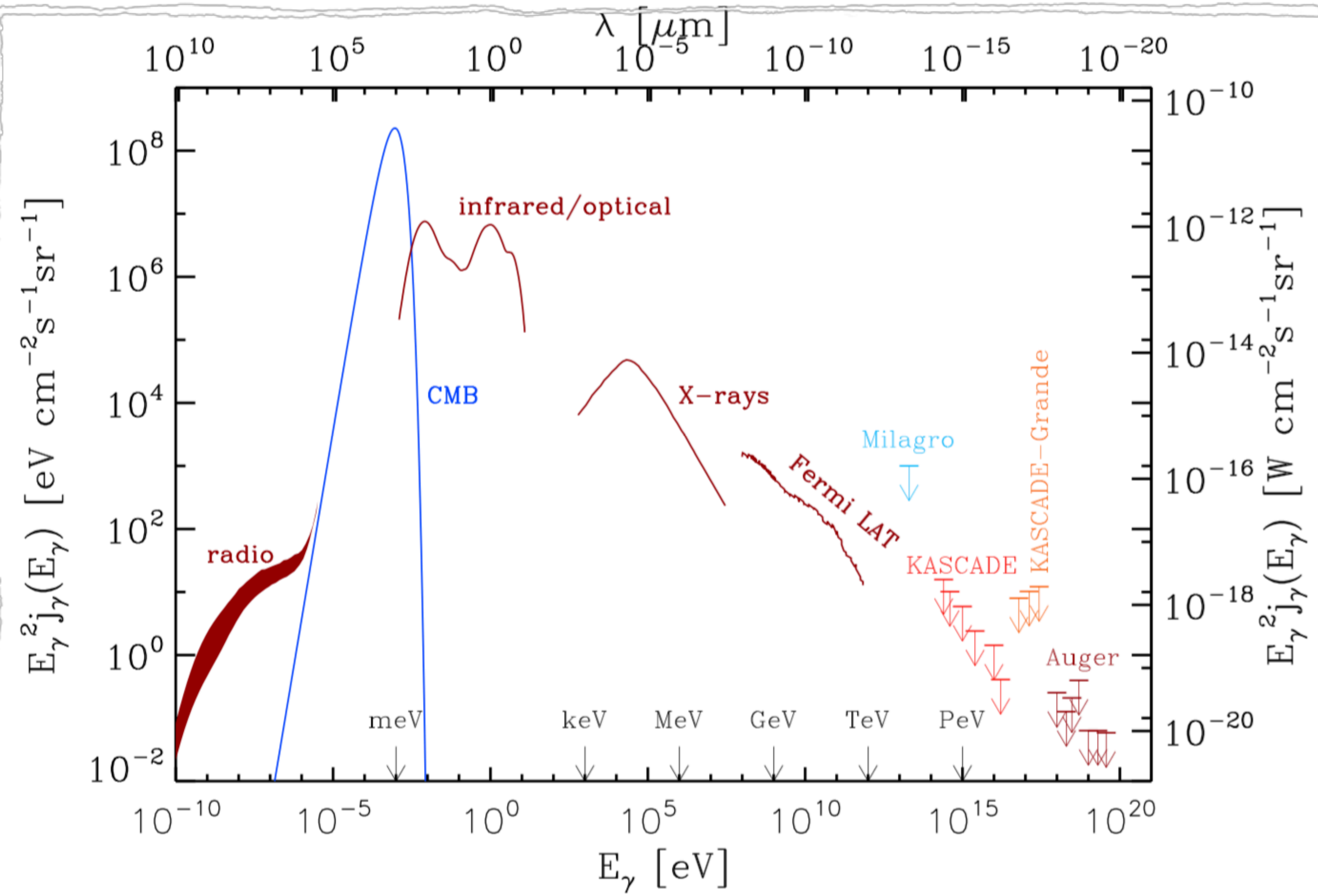

Fig. 5.16 The isotropic part of the diffuse "grand unified photon spectrum", represented as the energy flux as a function of energy (lower axis) or wavelength (upper axis). The arrows mark upper limits from the Milagro, the KASCADE [381], the KASCADE-Grande [382] and Pierre Auger experiments [383]. The CMB flux is calculated from Eq. (4.3) with $g = 2$ polarization degrees of freedom and $T_0 = 2.715\,\mathrm{K}$. Note that the energy flux per decade of energy, $E_\gamma^2 dN_\gamma/dE_\gamma = E_\gamma dN_\gamma/d\ln E_\gamma$, is plotted on the vertical axis. See also Ref. [384].

Multi-Messengers: The Big Picture

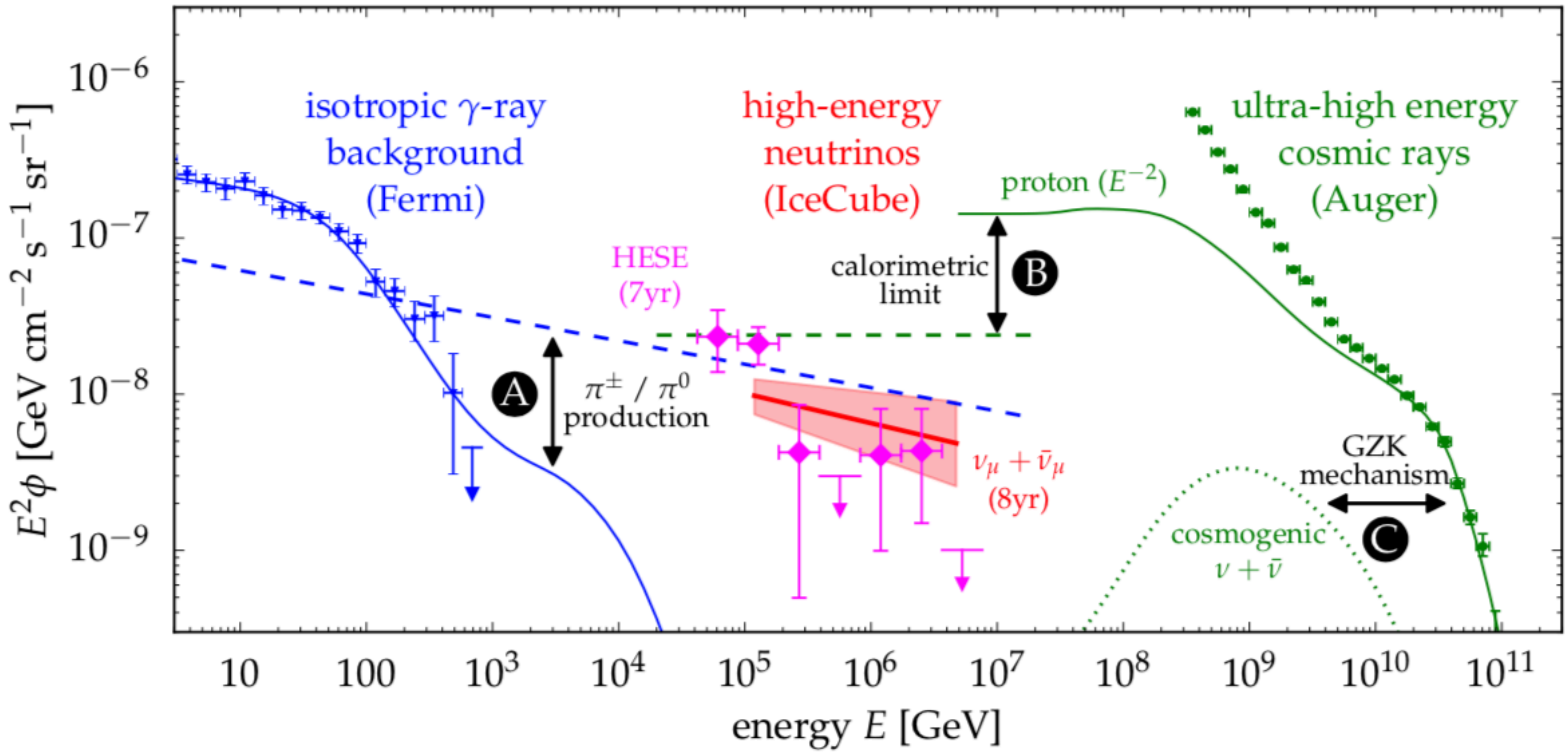

M. Ahlers, arXiv:1811.07633

Figure 1. The spectral flux (ϕ) of neutrinos inferred from the eight-year upgoing track analysis (red fit) and preliminary results of the seven-year HESE analysis [8] (magenta data) compared to the flux of unresolved extragalactic γ-ray sources [10] (blue data) and ultra-high-energy cosmic rays [11] (green data). The $\nu_\mu + \bar{\nu}_\mu$ spectrum is indicated by the best-fit power-law (solid line) and 1σ uncertainty range (shaded range). We highlight the various multimessenger relations: **A:** The joined production of charged pions ($\pi^{\pm}$) and neutral pions (π^0) in cosmic-ray interactions leads to the emission of neutrinos (dashed blue) and γ-rays (solid blue), respectively. **B:** Cosmic ray emission models (solid green) of the most energetic cosmic rays imply a maximal flux (calorimetric limit) of neutrinos from the same sources (green dashed). **C:** The same cosmic ray model predicts the emission of cosmogenic neutrinos from the collision with cosmic background photons (GZK mechanism).

1st Order Fermi Shock Acceleration

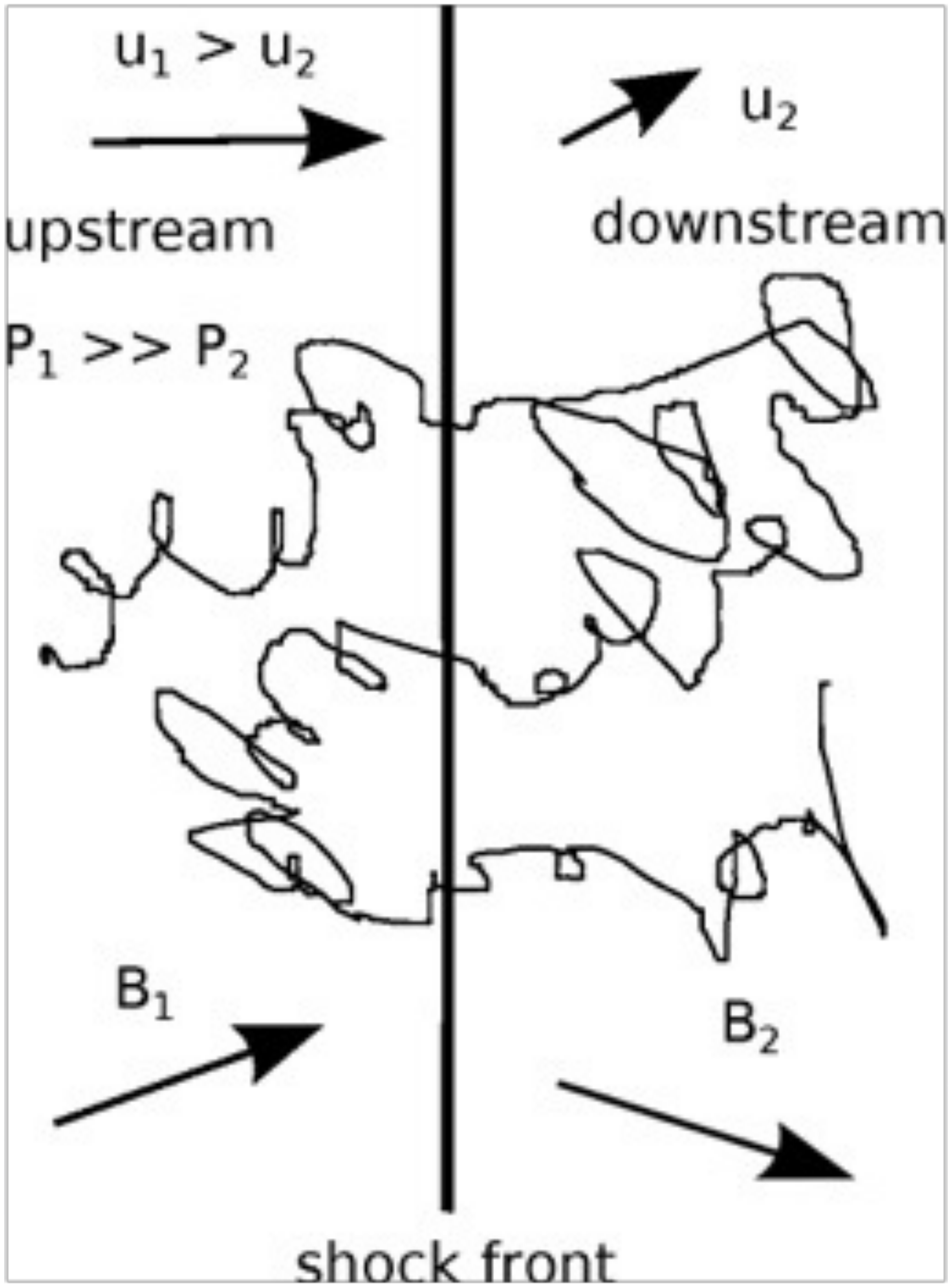

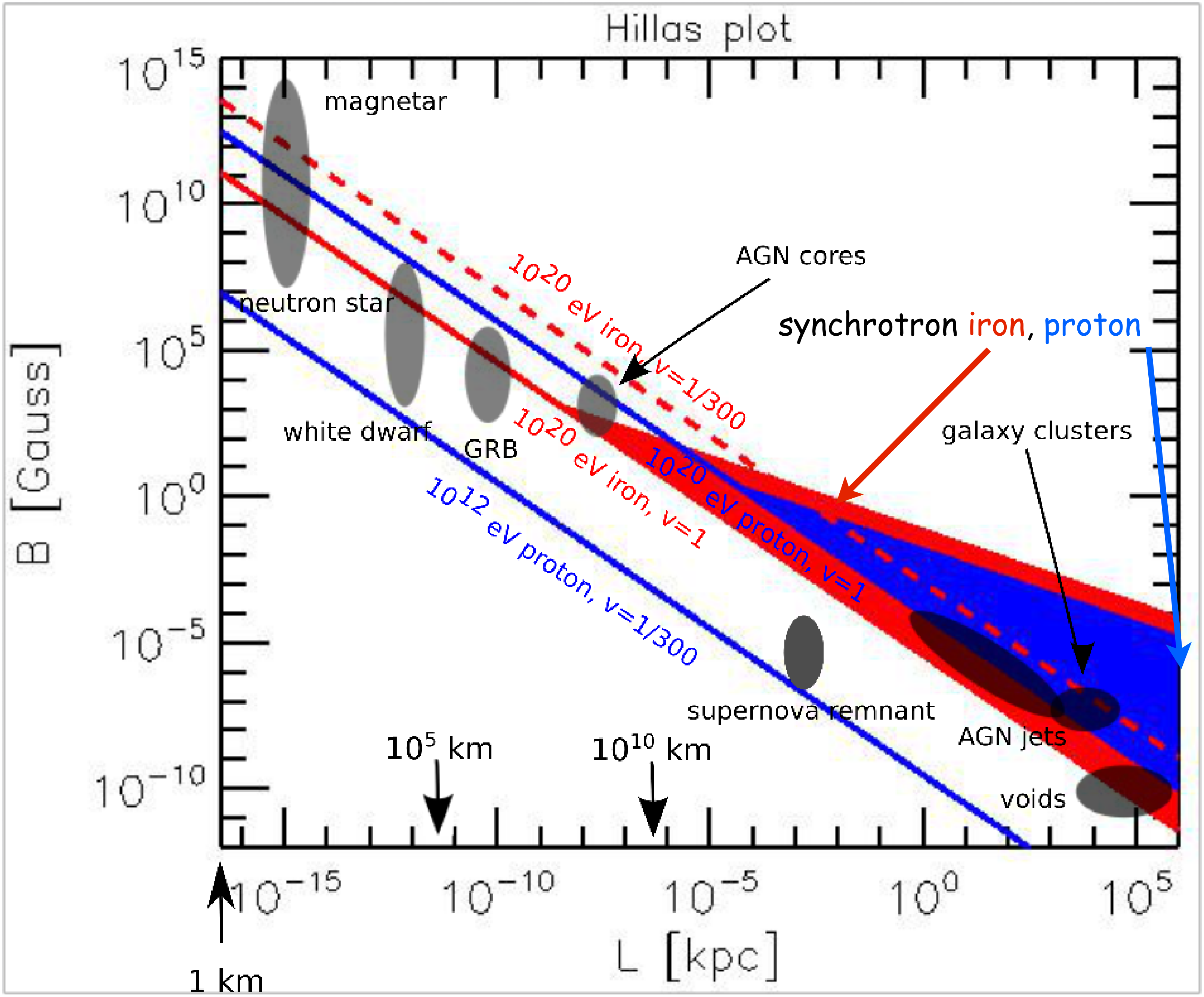

Fractional energy gain per shock crossing $\sim u_1 - u_2$ on a time scale r_L/u_2 .

Together with downstream losses this leads to a spectrum E^{-q} with $q > 2$ typically.

Confinement, gyroradius < shock size, and energy loss times define maximal energy

Some general Requirements for Sources

Accelerating particles of charge eZ to energy E_{max} requires induction $\varepsilon > E_{max}/eZ$. With $Z_0 \sim 100\Omega$ the vacuum impedance, this requires dissipation of minimum power of

$$L_{\rm min} \sim \frac{\epsilon^2}{Z_0} \simeq 10^{45}\, Z^{-2} \left(\frac{E_{\rm max}}{10^{20}\,{\rm eV}}\right)^2 \,{\rm erg\,s^{-1}}$$

This „Poynting" luminosity can also be obtained from $L_{min} \sim (BR)^2$ where BR is given by the „Hillas criterium":

$$BR > 3\times 10^{17}\,\Gamma^{-1}\left(\frac{E_{\rm max}/Z}{10^{20}\,{\rm eV}}\right)\,{\rm Gauss\,cm}$$

where Γ is a possible beaming factor.
If most of this goes into electromagnetic channel, only AGNs and maybe gamma-ray bursts could be consistent with this.

A possible acceleration site associated with shocks in hot spots of active galaxies

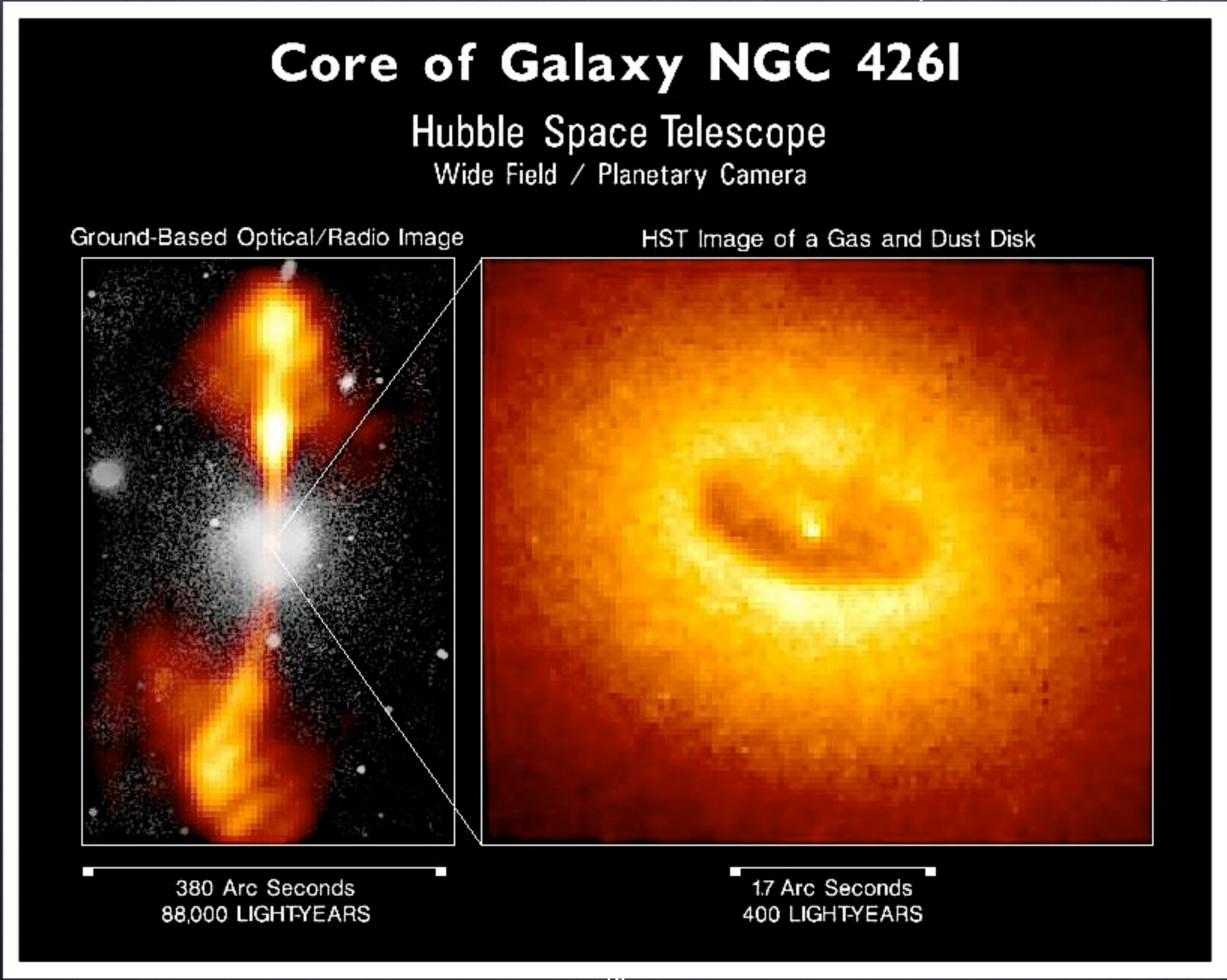

Or Cygnus A

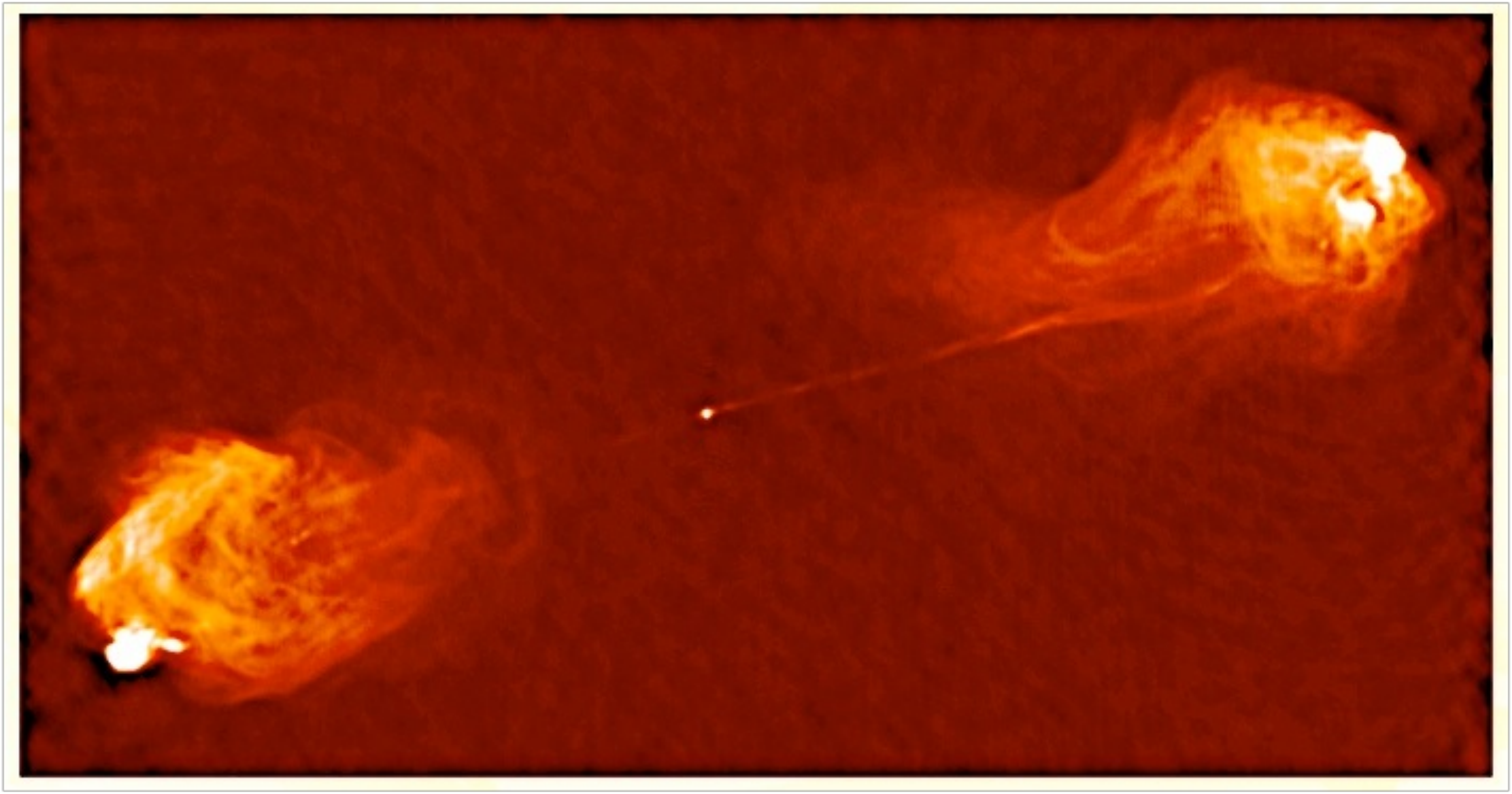

Mass Composition

Depth of shower maximum X_{max} and its distribution contain information on primary mass composition

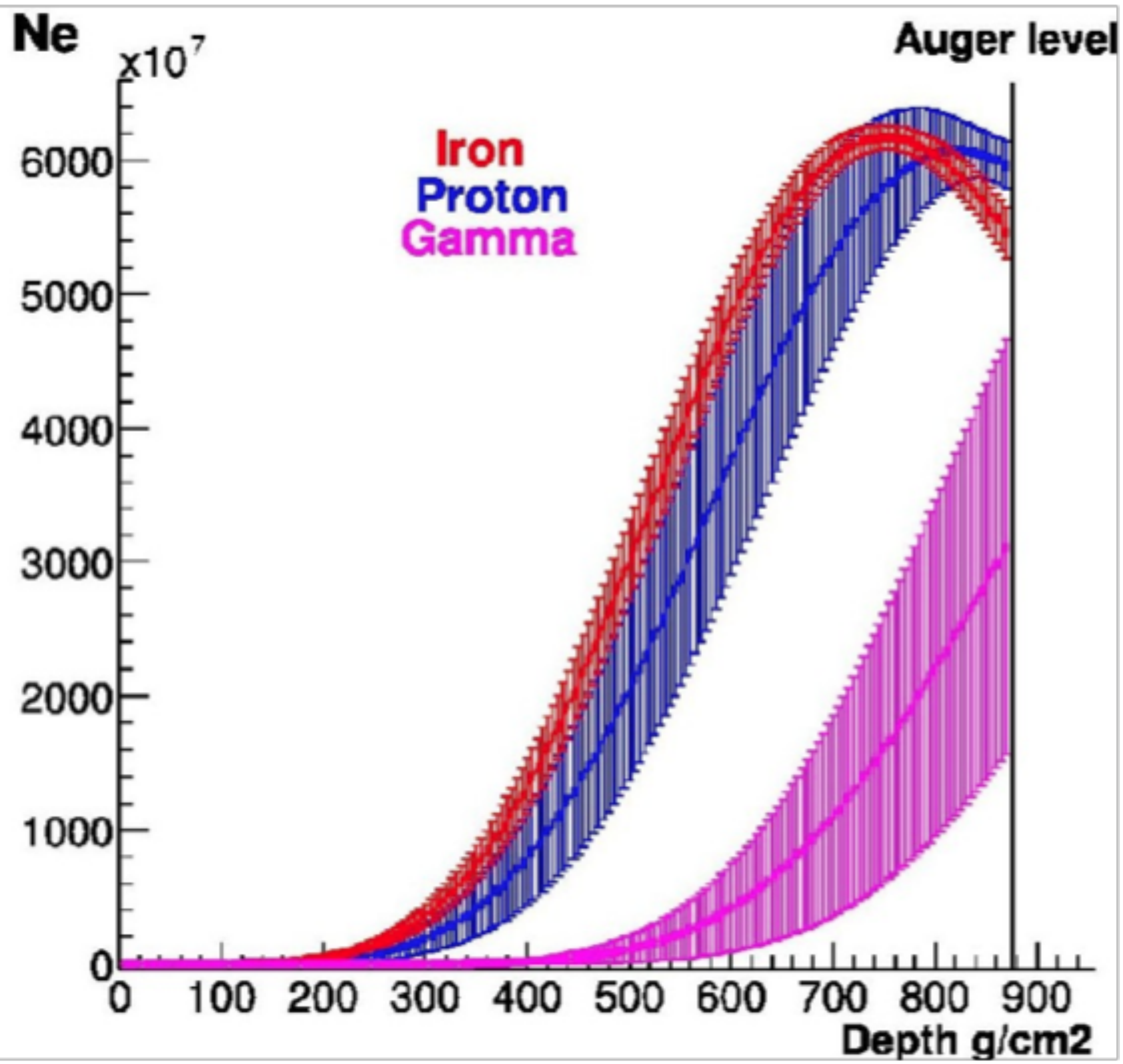

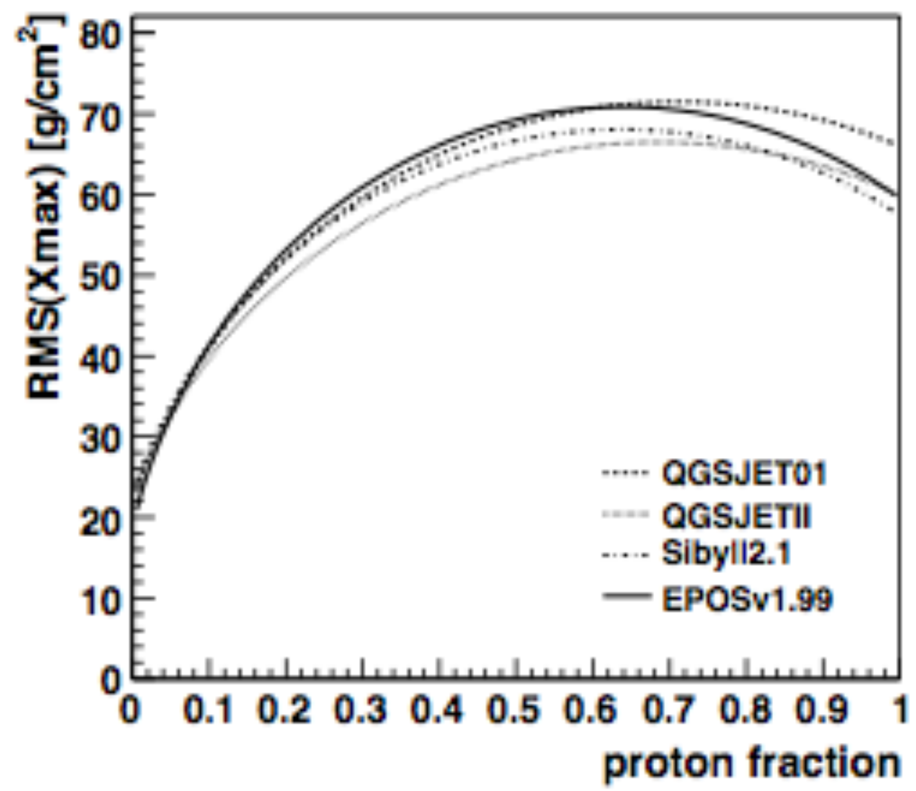

FIGURE 1. RMS(X_{max}) from different hadronic interaction models [23] and a two-component p/Fe composition model ($E = 10^{18}$ eV).

Muon number measured at 1000 m from shower core systematically higher than predicted

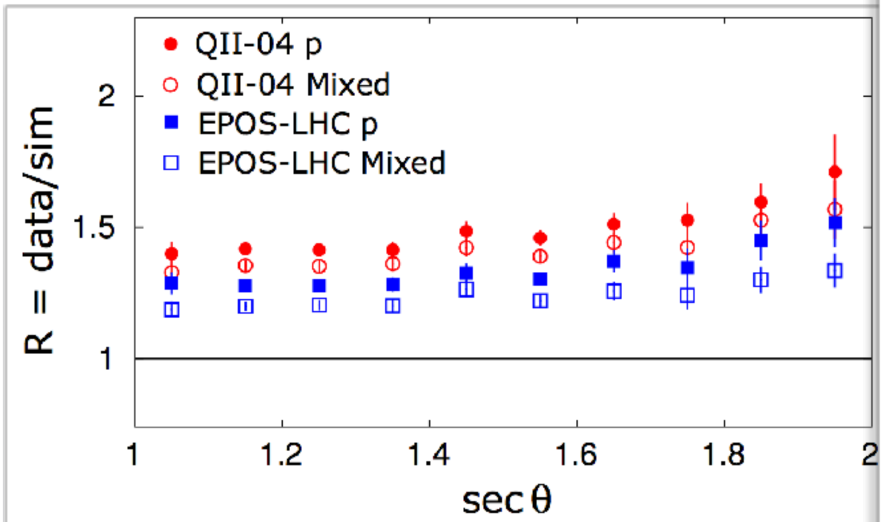

FIG. 2. The average ratio of S(1000) for observed and simulated events as a function of zenith angle, for mixed or pure proton compositions.

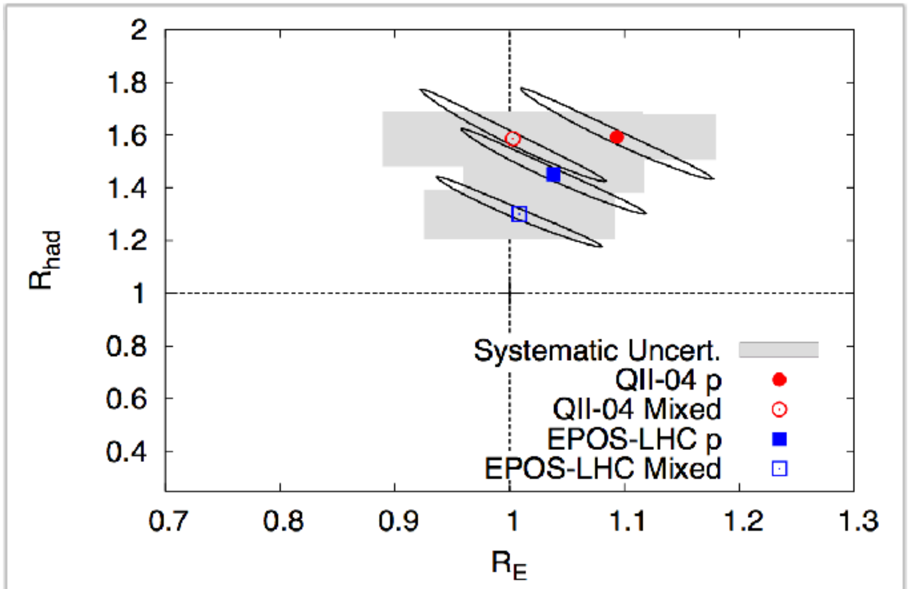

FIG. 4. Best-fit values of R_E and $R_{\rm had}$ for QGSJet-II-04 and EPOS-LHC, for pure proton (solid circle/square) and mixed composition (open circle/square). The ellipses and gray boxes show the 1-σ statistical and systematic uncertainties.

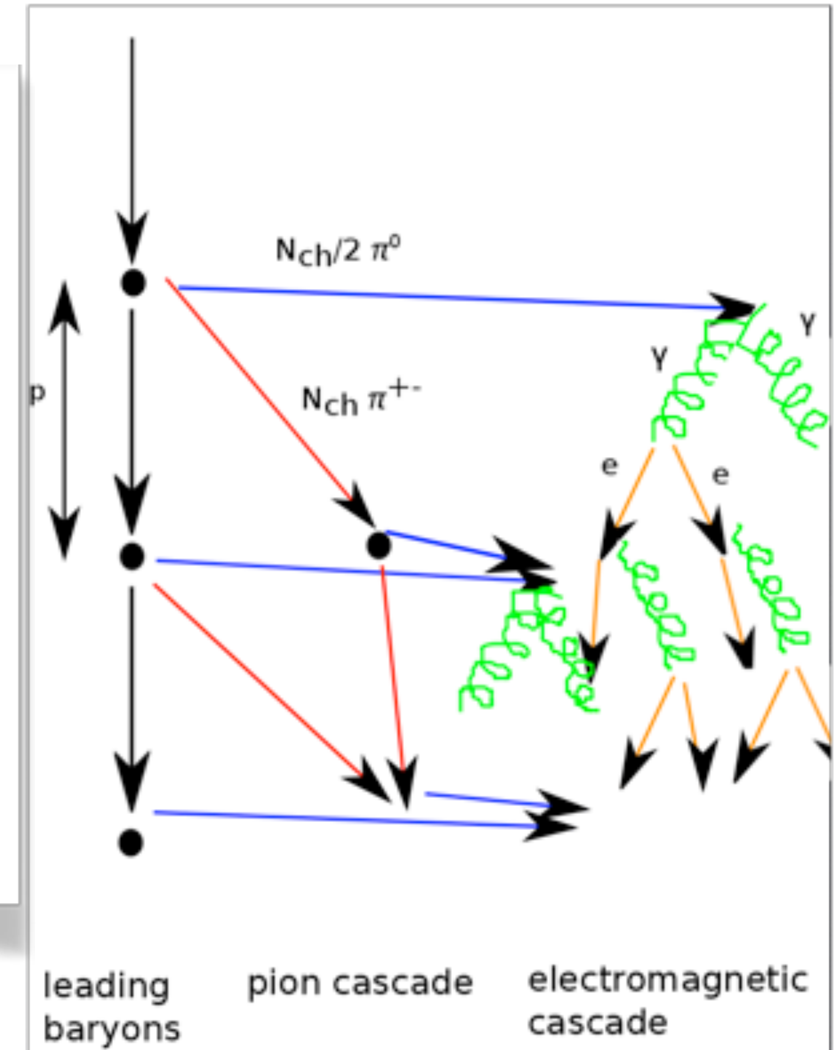

Pierre Auger Collaboration, PRL 117, 192001 (2016) [arXiv:1610.08509]

The muon number scales as

$$N_\mu \propto E_{\rm had} \propto (1 - f_{\pi^0})^N \ ,$$

with the fraction going into the electromagnetic channel $f_{\pi^0} \simeq \frac{1}{3}$ and the number of generations N strongly constrained by $X_{\rm max}$. Larger N_μ thus requires smaller f_{π^0} ! The production of ρ^0 could also play a role.

Spectrum and Composition

fits to spectrum and composition for a homogeneous source distribution neglecting deflection (which generally is a good approximation for the solid angle integrated flux) tend to favor very hard injection spectra with low cut-off rigidities

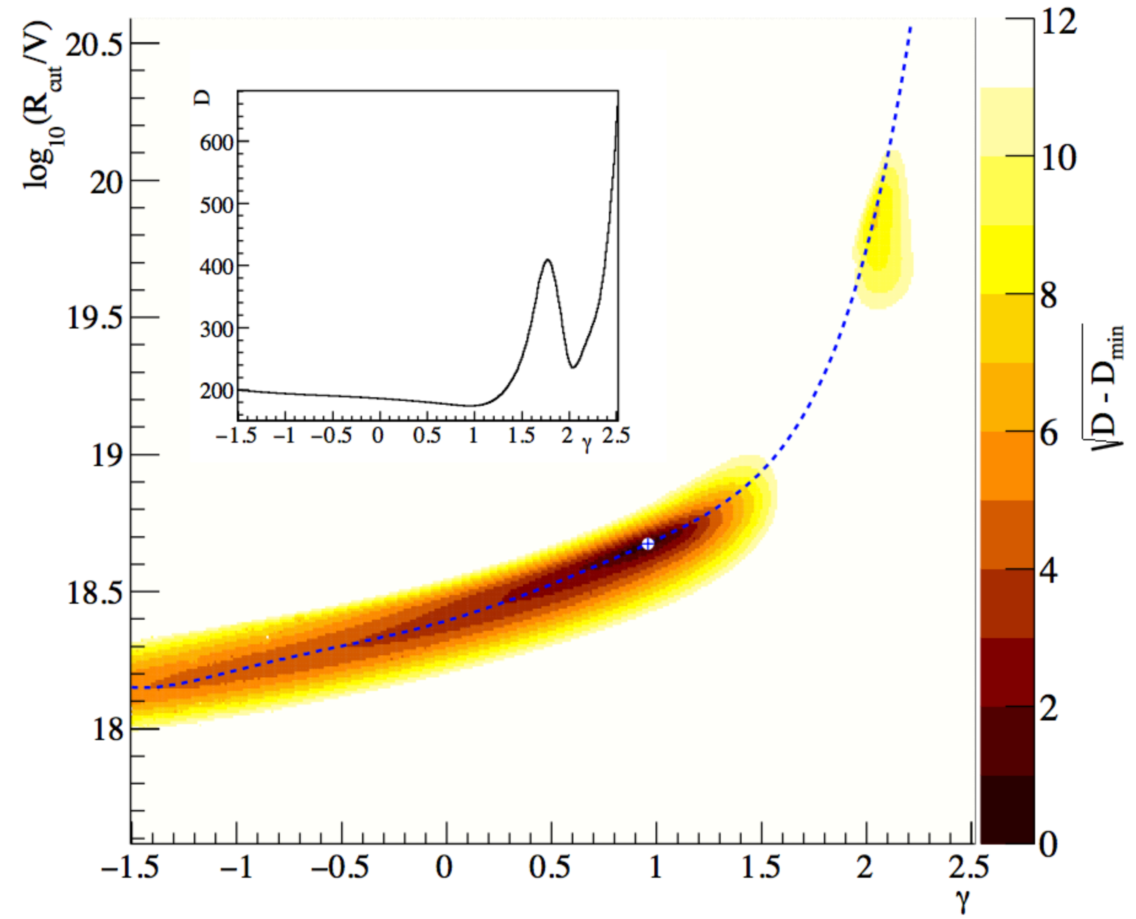

Pierre Auger collaboration, JCAP 1704 (2017) 028 [arXiv:1612.07155]

Figure 1. Deviance $\sqrt{D - D_{\rm min}}$, as function of γ and $\log_{10}(R_{\rm cut}/{\rm V})$. The dot indicates the position of the best minimum, while the dashed line connects the relative minima of D (valley line). In the inset, the distribution of $D_{\rm min}$ in function of γ along this line.

cutoff may be mostly caused by source physics; Peters cycle at highest energies is most "economic" in terms of source power.

Newest Results on Anisotropy

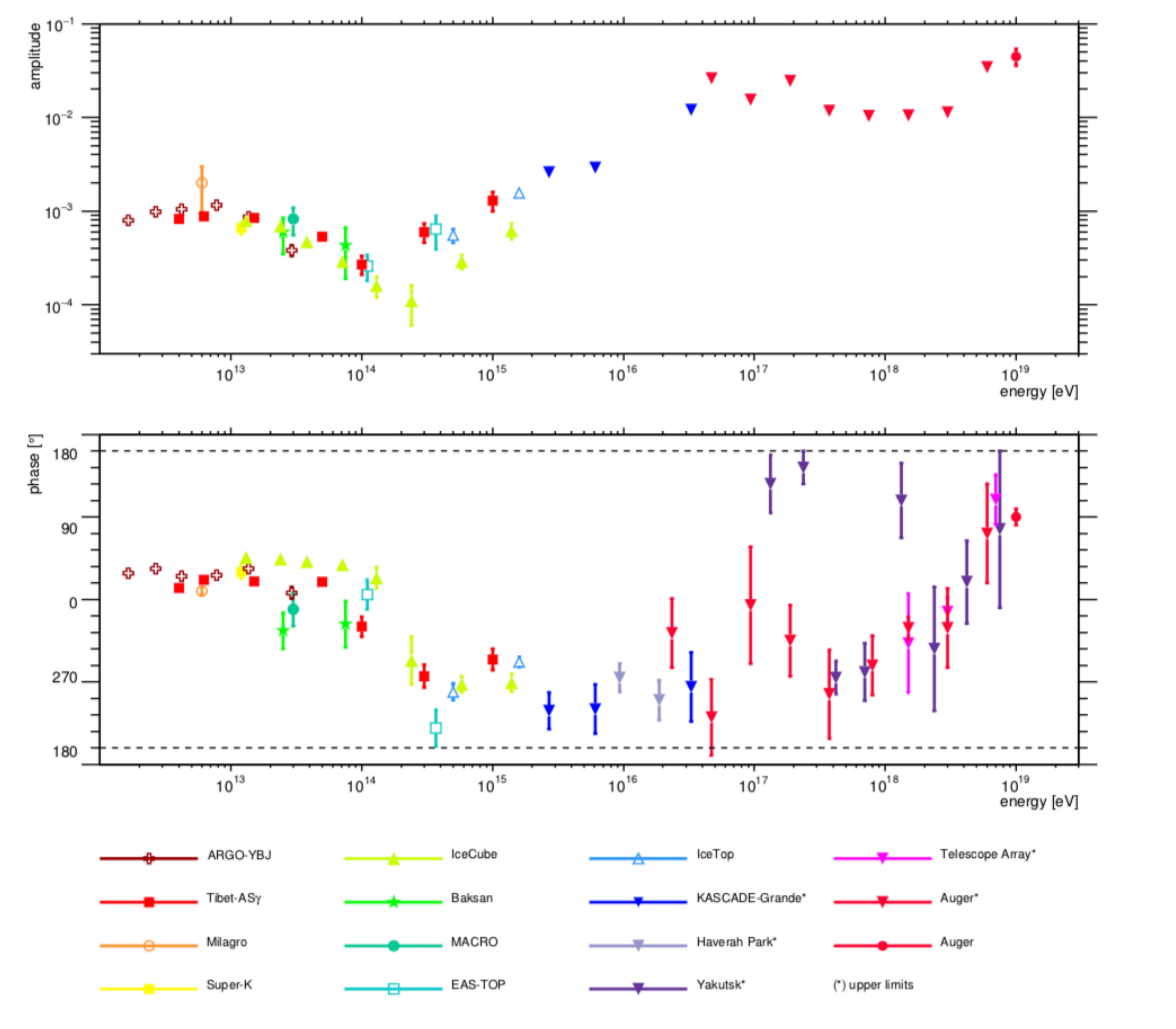

Figure 7: Amplitude (top) and phase (bottom) measurements of the first harmonic in right ascension as a function of energy, from various reports. Amplitudes drawn as triangles with apex pointing down are the most stringent upper limits up to date in the considered energy ranges.

Amplitude and phase of dipole as function of energy

O. Deligny, arXiv:1808.03940

A Significant Anisotropy around 8×10^{18} eV is now seen

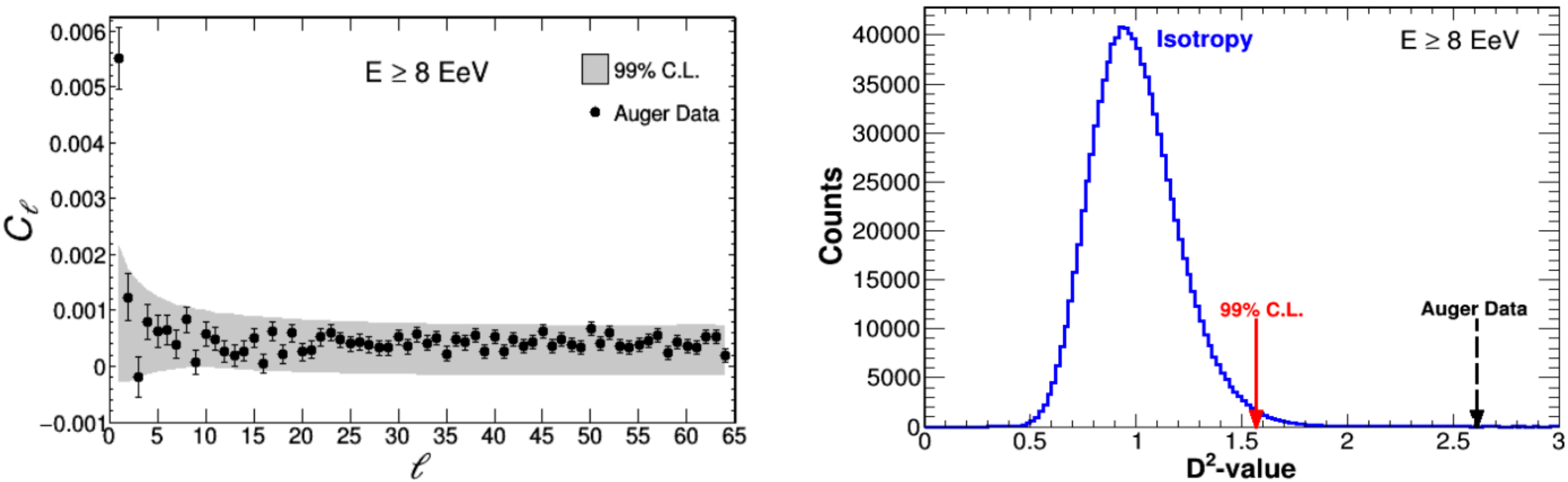

Figure 3: Angular power spectrum for $E \geq 8$ EeV. On the left a clear indication for a departure from isotropy is captured in the dipole scale. On the right the D^2-value distribution from 1,000,000 isotropic sky maps is shown. The D^2-value from data, represented by the black (dashed) arrow, is larger than the threshold of isotropy presenting an indication of anisotropy with $> 99\%$ C.L..

Pierre Auger Collaboration, JCAP 1706 (2017) 026 [arXiv:1611.06812]

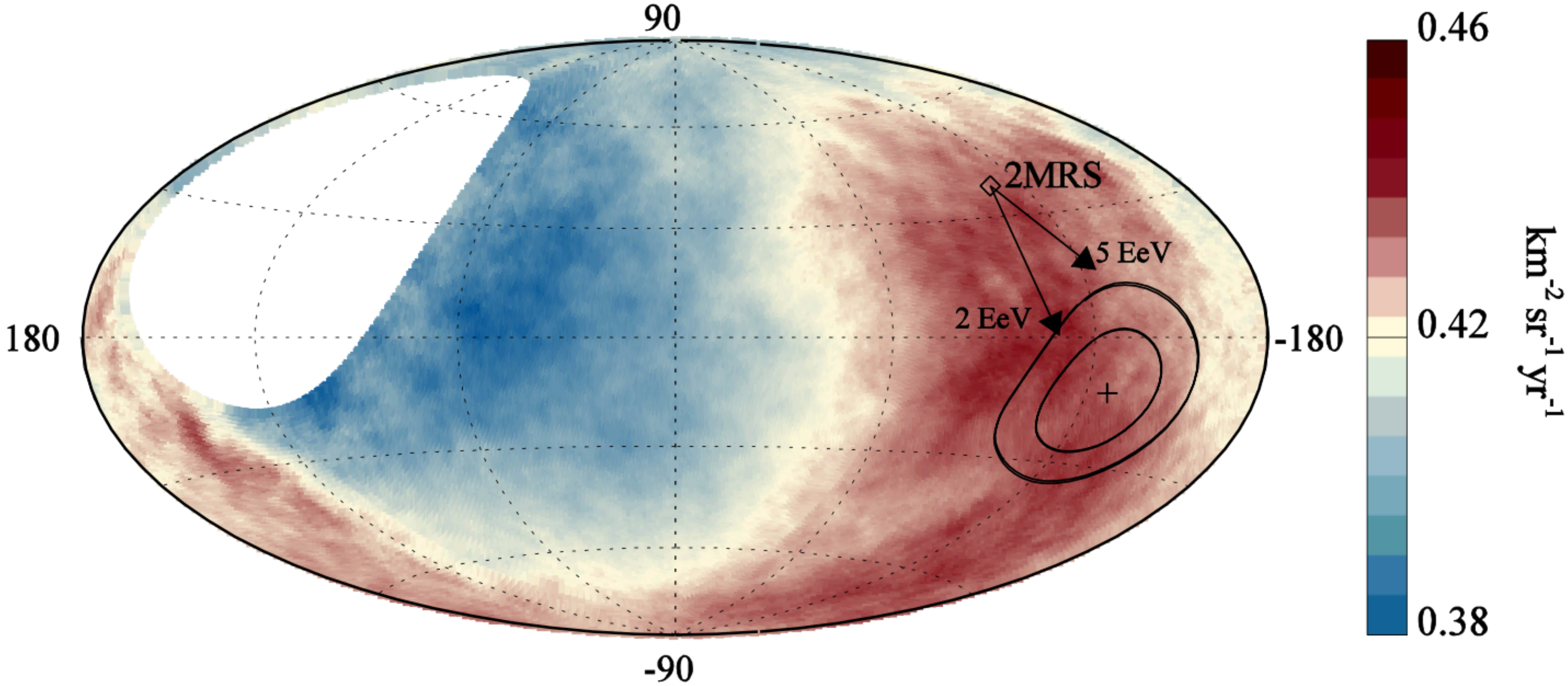

Fig. 3. Map showing the fluxes of particles in Galactic coordinates. Sky map in Galactic coordinates showing the cosmic-ray flux for $E \geq 8$ EeV smoothed with a 45° top-hat function. The Galactic center is at the origin. The cross indicates the measured dipole direction and the contours the 68% and 95% confidence-level regions. The dipole in the 2MRS galaxy distribution is indicated, while arrows show the deflections expected for a particular model of the Galactic magnetic field (*8*), for *E/Z*=5 EeV or 2 EeV.

Pierre Auger Collaboration, Science 357 (22 September 2017) 1266 [arXiv:1709:07321]

3-Dimensional Effects in Propagation

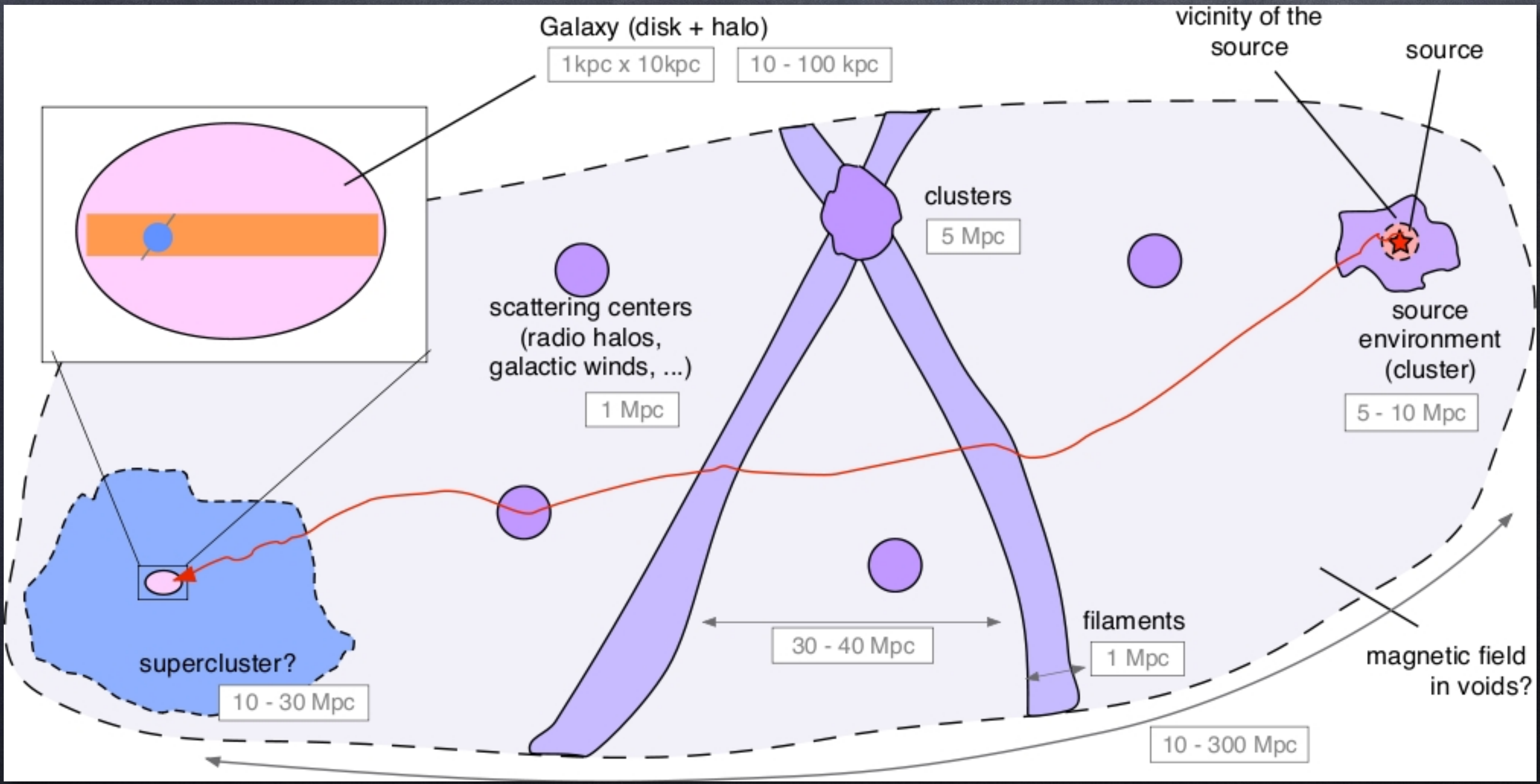

Kotera, Olinto, Ann.Rev.Astron.Astrophys. 49 (2011) 119

Modelling Challenges

- Broad dynamic range in length and time scales
- partly unknown propagation mode: ballistic versus diffusive
- disentangling source distribution/rates from propagation mode

Reminder: Propagation Theorem/Liouville Theorem

A homogeneous distribution of sources with equal properties and nearest neighbour distances smaller than other relevant length scales in the problem such as energy loss length and propagation/diffusion length within the source activity time scale gives rise to a universal/isotropic flux spectrum that does not depend on the propagation mode and thus on the magnetic field properties.

Easiest to see in the back-tracking picture:

The differential flux in the direction characterised by the unit vector $\mathbf{n}$ at observer position $\mathbf{r}_0$ is given by

$$j(E_0, \mathbf{r}_0, \mathbf{n}) = \int_{t_0}^{t_{\max}} dt \dot{\rho}\left[E(t), t, \mathbf{r}(t, \mathbf{n})\right] \,,$$

where $\dot{\rho}(E, t, \mathbf{r})$ is the differential injection rate at energy E, time t, and location $\mathbf{r}$, $\mathbf{r}(t, \mathbf{n})$ is the back-tracked trajectory with the initial conditions $\mathbf{r}(t_0, \mathbf{n}) = \mathbf{r}_0$, $\dot{\mathbf{r}}(t_0, \mathbf{n}) = \mathbf{n}$ and $E(t)$ with $E(t_0) = E_0$ is the back-tracked energy. For stochastic losses one has to average over trajectories with equal initial conditions.

Clearly, if $\dot{\rho}$ only depends on E and t, then the flux neither depends on the shape of the trajectories nor on direction, but only on energy, and thus is universal.

This also applies to secondary fluxes such as neutrinos and gamma-rays because densities only depend on the time-integrated interaction rates (and energy loss rates) which are location independent

Corollary:

To be sensitive to the propagation mode, magnetic field structure etc. requires discrete, inhomogeneous source distributions with nearest-neighbour distances larger than energy loss length and/or propagation distance within source activity time

A Simple One Source + Isotropic Background Model

Contribution of the one discrete source to the total flux parametrised by η and deflection spread by concentration parameter κ: Dipole and quadrupole can fix both parameters, e.g. C_2/C_1 fixes κ

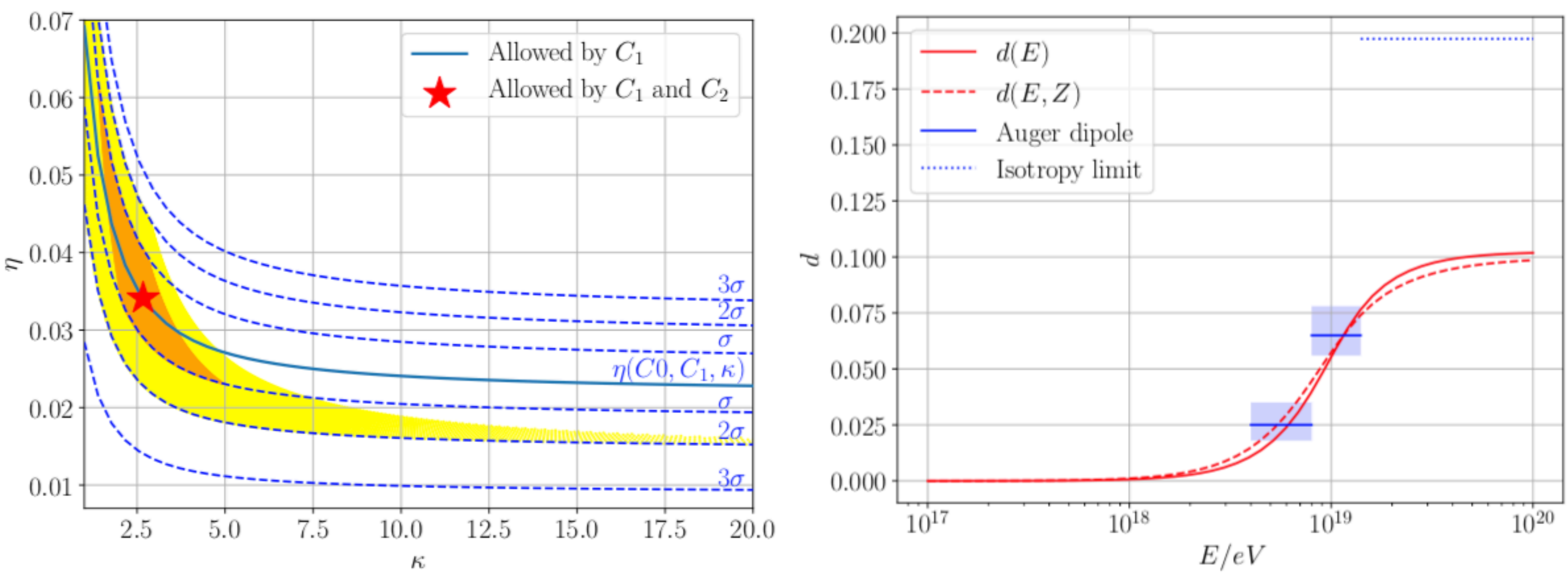

Dundovic and Sigl, arXiv:1710.05517

Dundovic and Sigl, arXiv:1710.05517

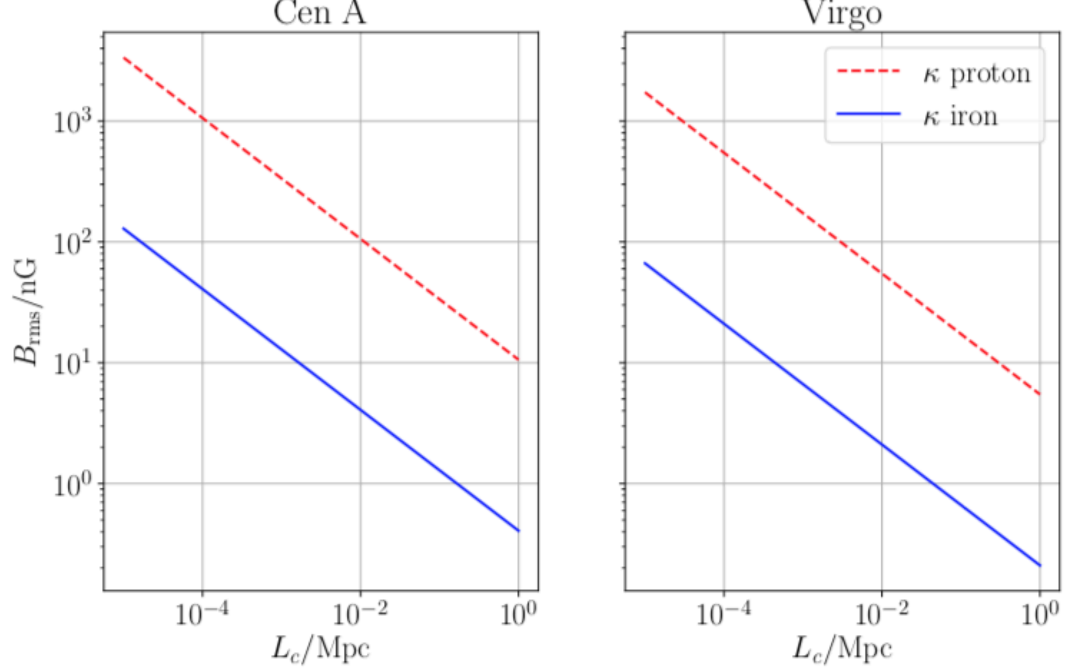

Figure 12. For a source of a given distance, the remaining parameters left undetermined are charge, magnetic field strength and coherence length. The plot shows the relation between $B_{\rm rms}$ and L_c following from eq. 3.4 for the fitted value of κ, for proton and iron primaries coming from Centaurus A and the Virgo cluster.

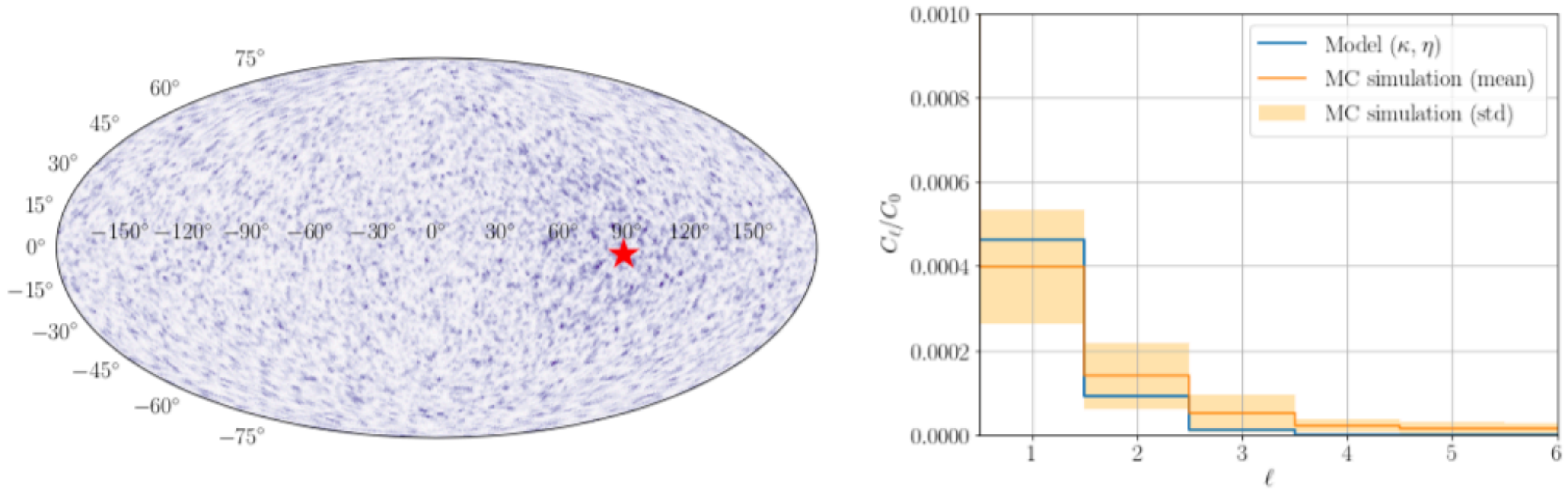

Figure 13. The two plots are results of a Monte Carlo simulation which is set up as described in the text. The sky plot shows the dipole induced by the single source which is placed at 4 Mpc distance from the observer. The direction of the dipole is marked with the star. Other parameters are $Z = 26$, $E = 11.5EeV$, $B_{\rm rms} = 2.9\,{\rm nG}$, $L_c = 30\,{\rm kpc}$, $\eta = 0.03$ where $(1 - \eta)$ is the isotropic contribution from the background. The right panel plot depicts the first few moments of the angular power spectrum where the blue line is the analytically calculated spectrum by using the spread parameter (κ) and the relative flux (η), while the orange line is a fit from the simulation. The orange shaded area represents one sigma fluctuations.

Extragalactic Magnetic Field Filling Factors from recent Simulations

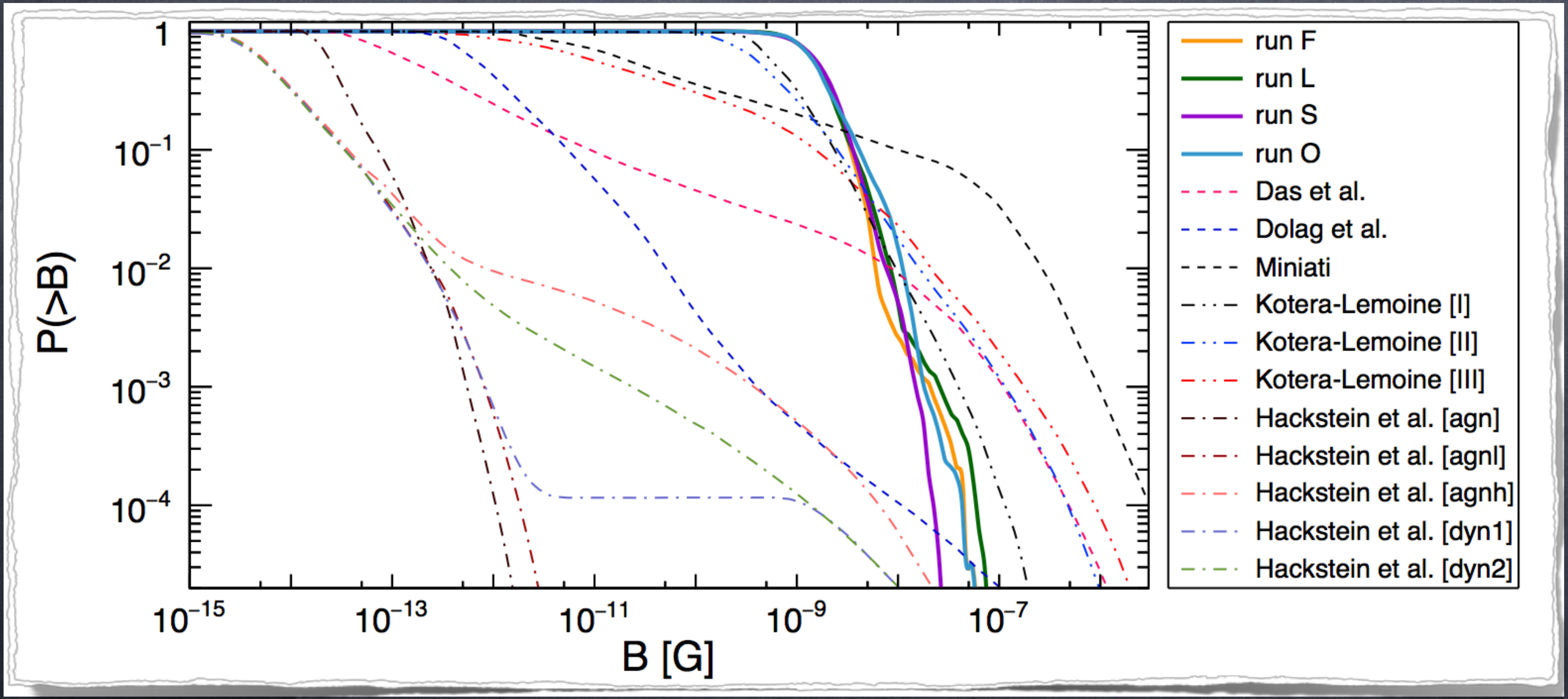

Alves Batista et al, PRD 96 (2017) 023010 [arXiv:1704.05869]

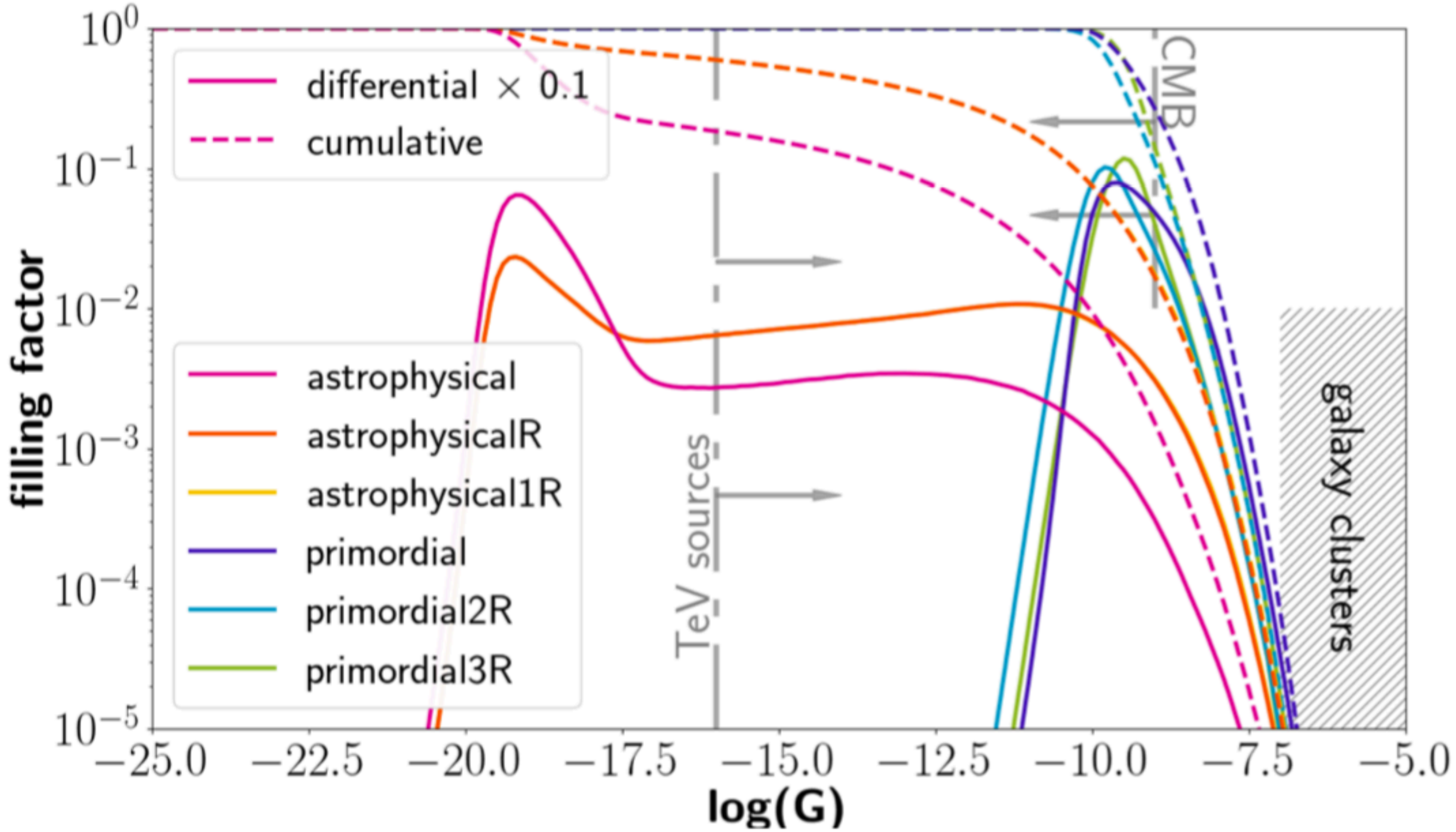

Figure 2. Volume filling factor of the models listed in Tab. 1. The solid lines show the differential filling factor renormalized by 0.1 for clarity, dashed lines show the cumulative filling factor. The grey arrows and shaded area indicate the limits given from observations as listed in the introduction. The yellow line of the *astrophysical1R* model fits exactly with the *astrophysicalR* model.

Hackstein et al., Mon.Not.Roy.Astron.Soc. 475 (2018) no.2, 2519 [arXiv:1710.01353]

Extragalactic iron propagation produces nuclear cascades in structured magnetic fields:

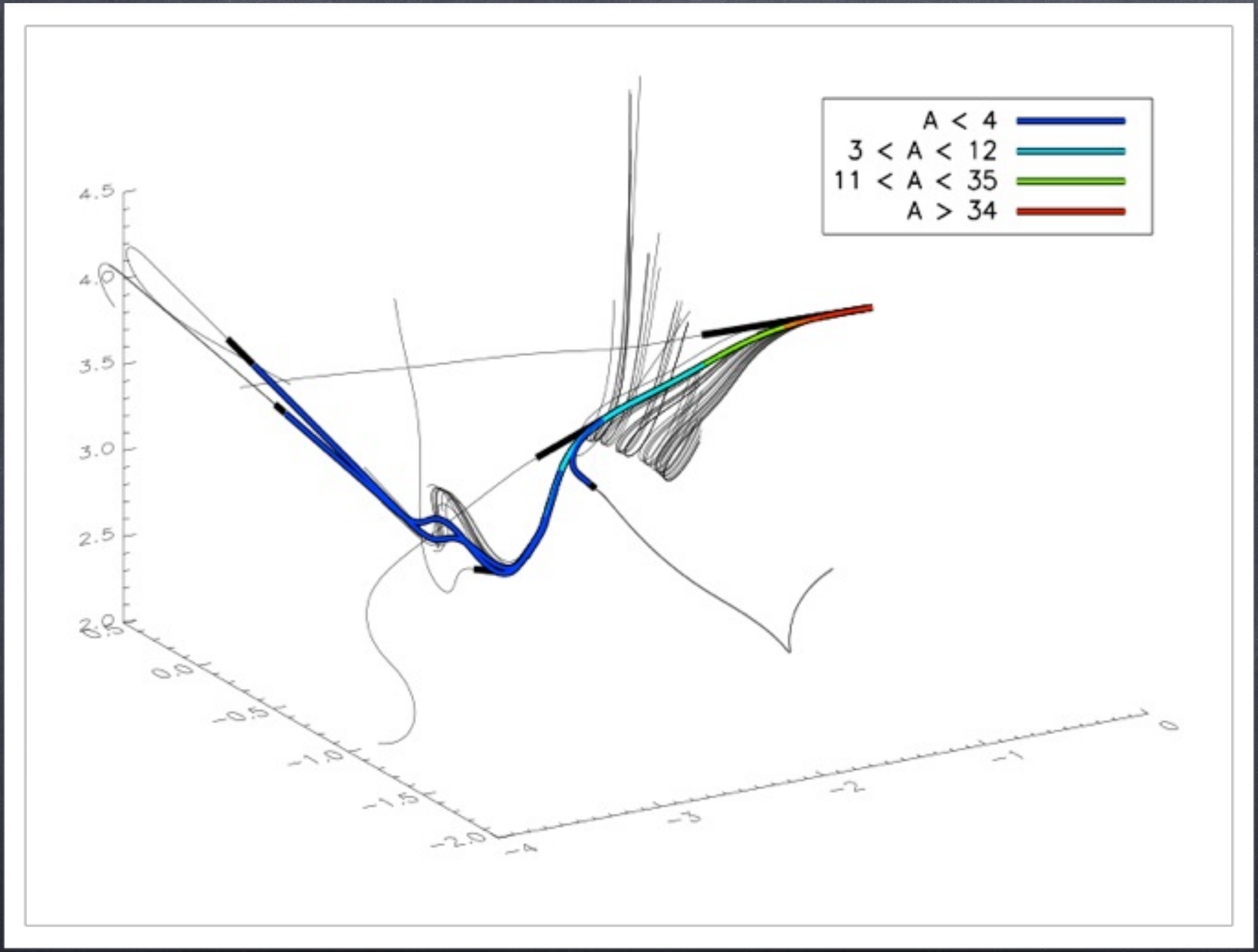

Initial energy 1.2 x 10^{21} eV, magnetic field range 10^{-15} to 10^{-6} G. Color-coded is the mass number of secondary nuclei

CRPropa 2.0/3.0

CRPropa is a public code for UHE cosmic rays, neutrinos and γ-rays being extended to heavy nuclei and hadronic interactions

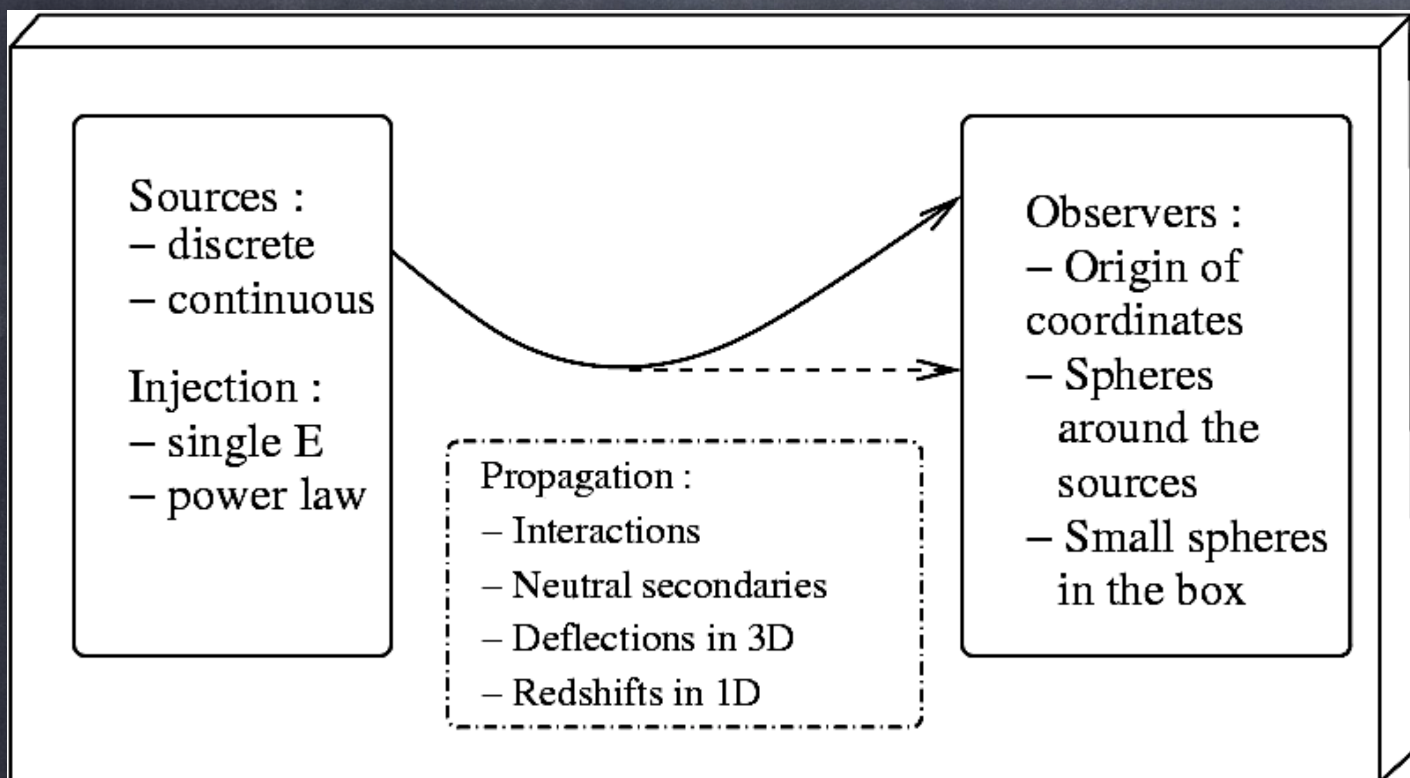

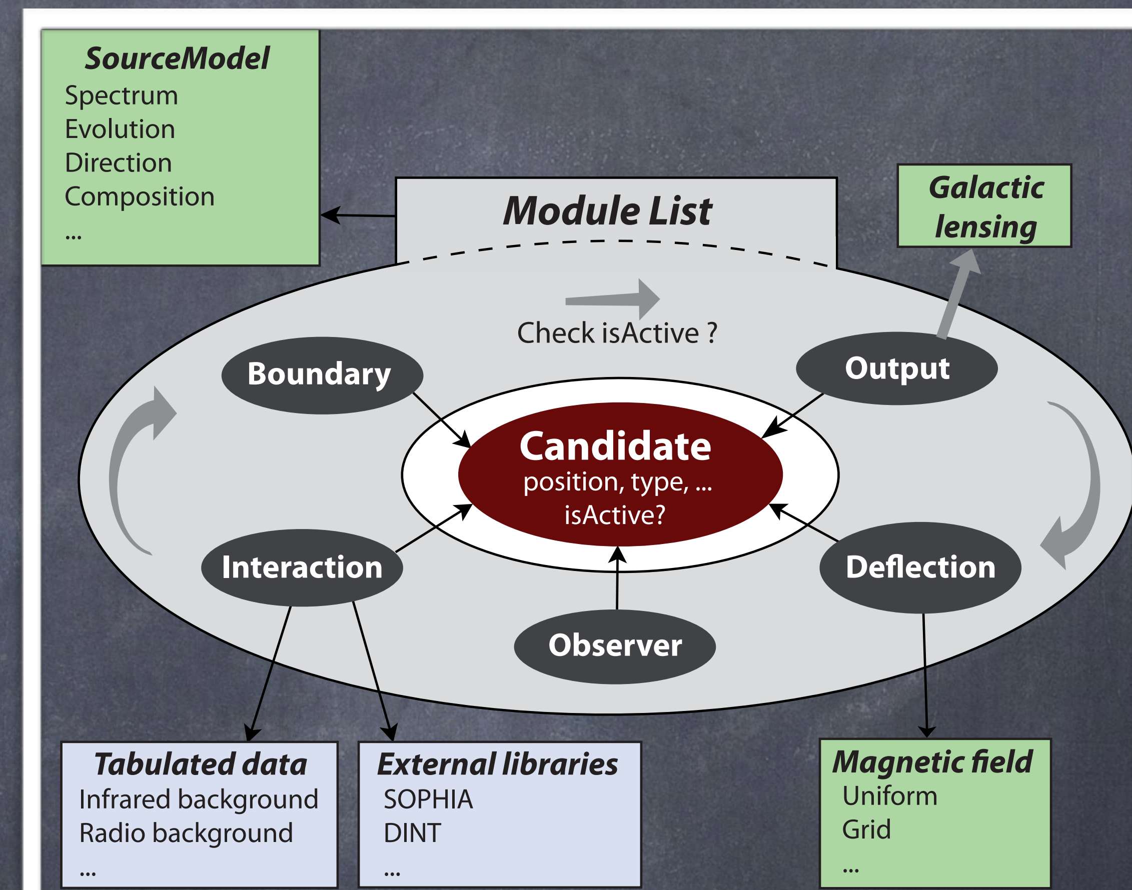

Version 1.4: Eric Armengaud, Tristan Beau, Günter Sigl, Francesco Miniati,
Astropart.Phys.28 (2007) 463.

https://crpropa.desy.de/Main_Page

https://github.com/CRPropa/CRPropa3/

Version 2.0: Luca Maccione, Rafael Alves Batista, David Walz, Gero Müller, Nils Nierstenhoefer, Karl-Heinz Kampert, Peter Schiffer, Arjen van Vliet
Astroparticle Physics 42 (2013) 41

Discrete Sources in nearby large scale structure

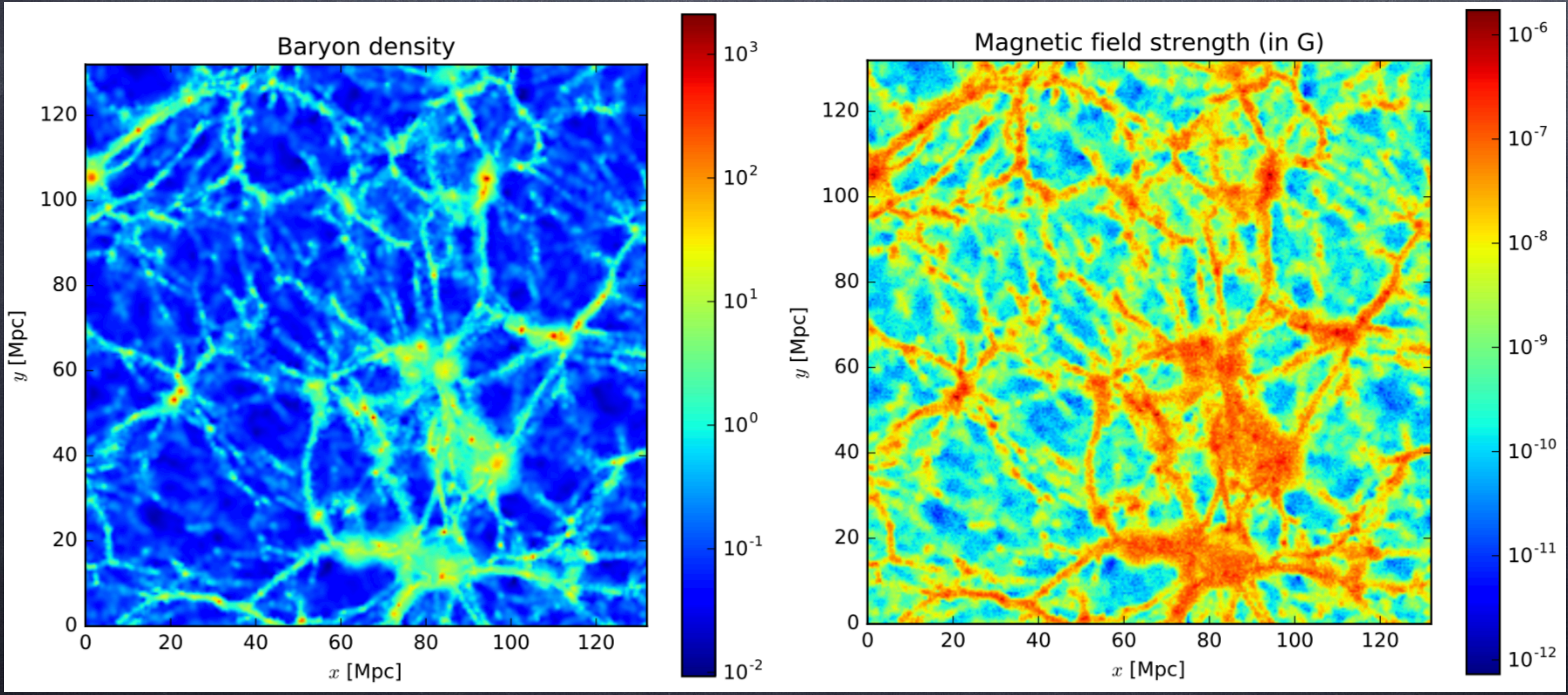

Building Benchmark Scenarios

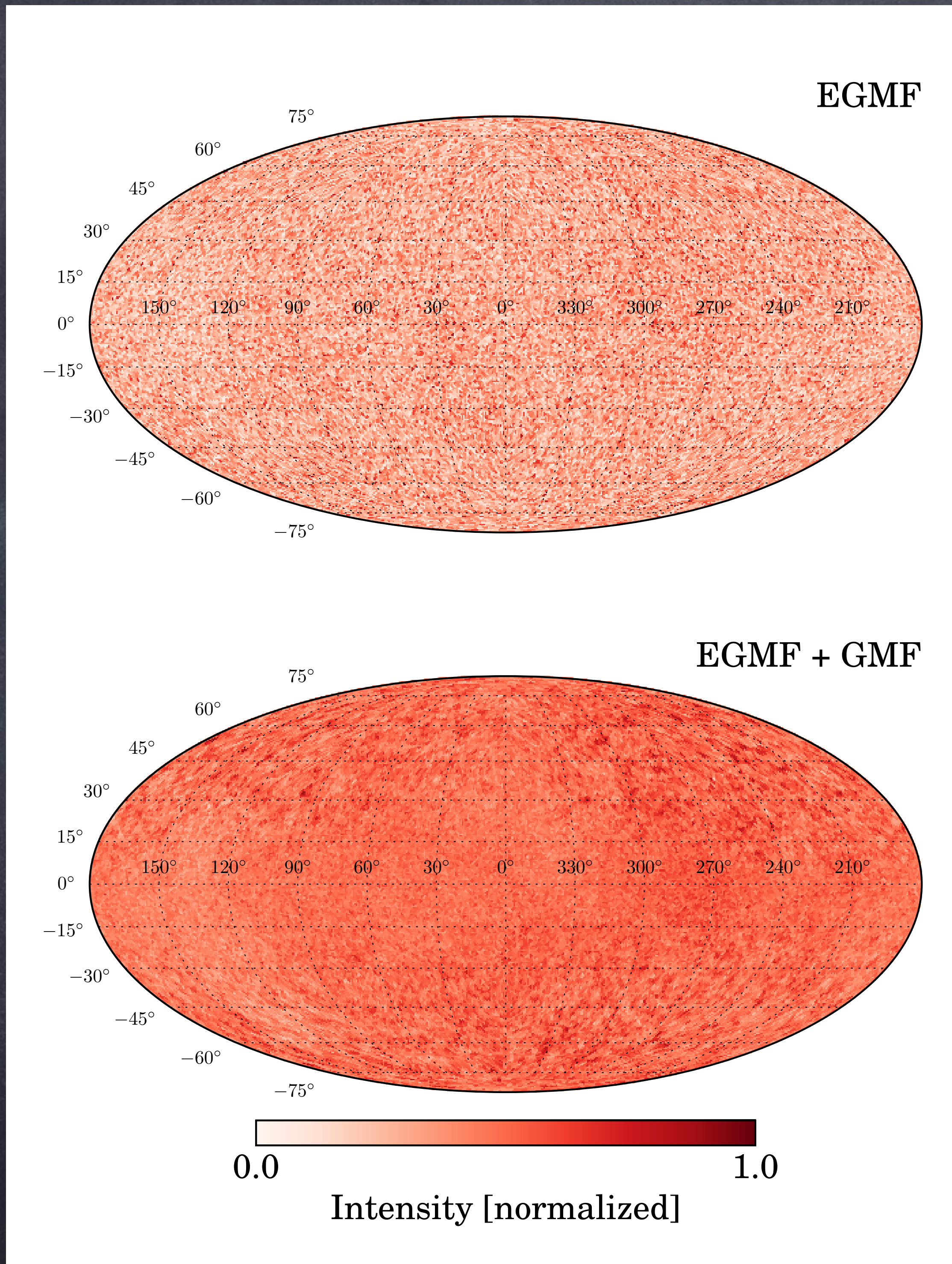

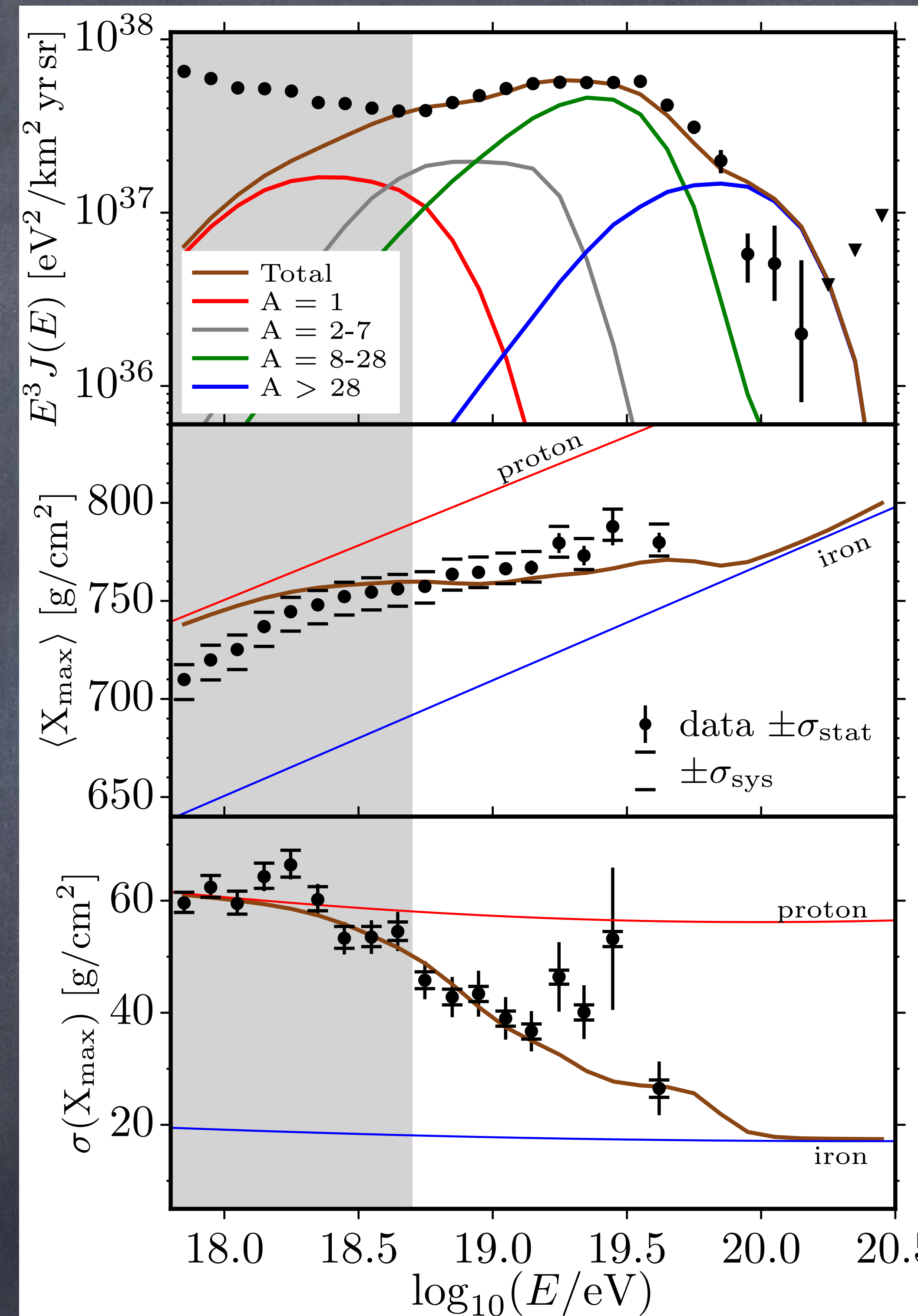

combining spectral and composition information with anisotropy can considerably strengthen constraints on source characteristics, distributions and magnetization

Simulated Predictions of angular Multipoles

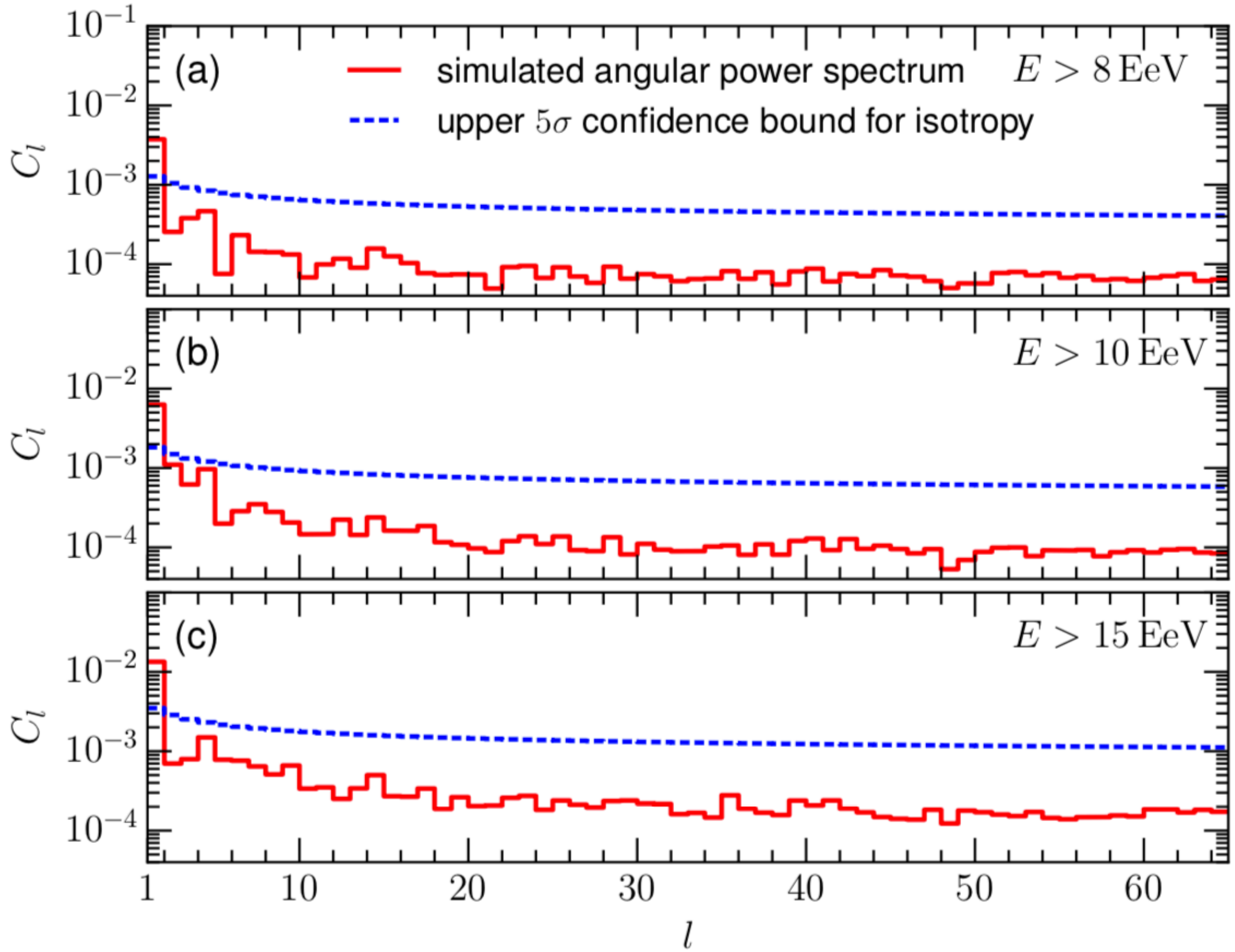

Figure 1. Angular power spectrum (solid red curves) for the arrival directions of the simulated UHECR reaching the observer with energies (a) $E > 8\,\mathrm{EeV}$, (b) $E > 10\,\mathrm{EeV}$, and (c) $E > 15\,\mathrm{EeV}$ as well as the corresponding upper 5σ confidence bounds for isotropy (dashed blue curves). For all energy intervals there is a significant dipolar anisotropy (see the values of $C_1(E)$), whereas the higher-order $C_l(E)$ are compatible with isotropy.

Wittkowski, Kampert, Astrophys. J. 854 (2018) L3 [arXiv:1710.05617]

based on the "benchmark model" which combines constrained large scale structure simulation with magnetic field strength distribution of Miniati model

inclusion of EGMF also leads to softer best fir injection indices γ ~ 1.6 [Wittkowski, proceedings of ICRC 2017]

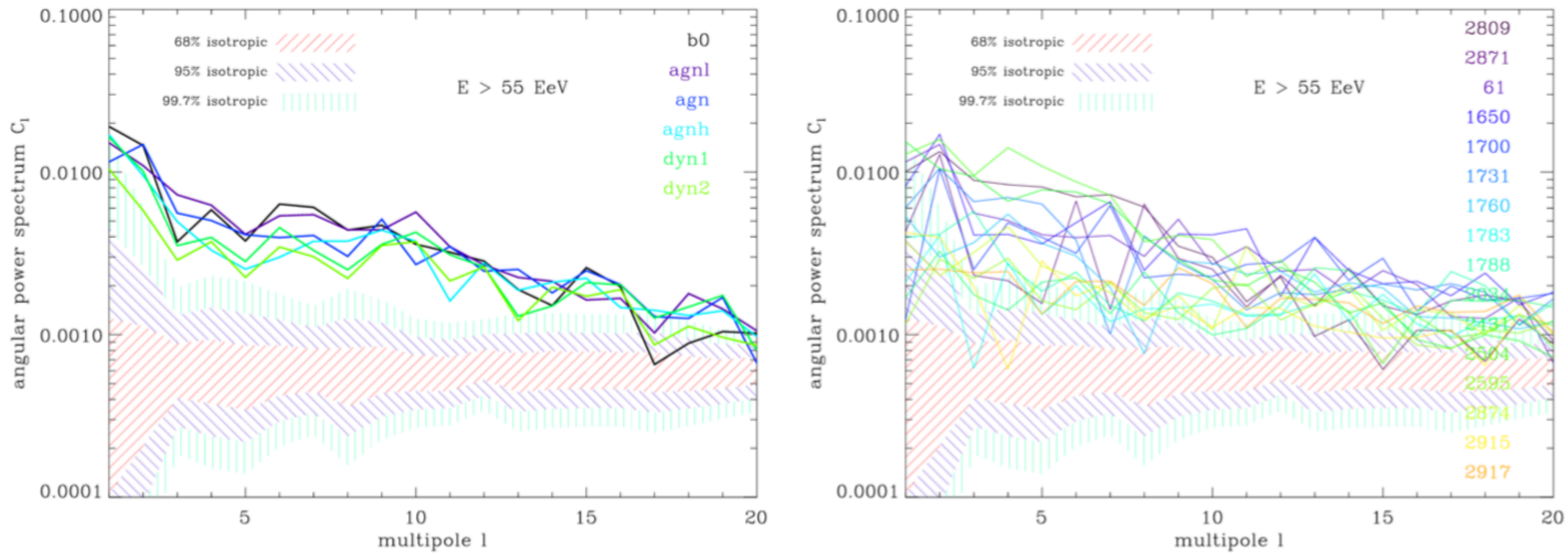

Figure 9. Left: Angular power spectrum of UHECR events observed by ID61 with energies $E > 55$ EeV for the different magnetic field models. Right: same as left, all 16 observers in one model (*agn*).

based on ENZO simulations

Hackstein, Vazza, Brüggen, Sigl, Dundovic,
Mon.Not.Roy.Astron.Soc. 462 (2016) no.4, 3660 [arXiv:1607.08872]

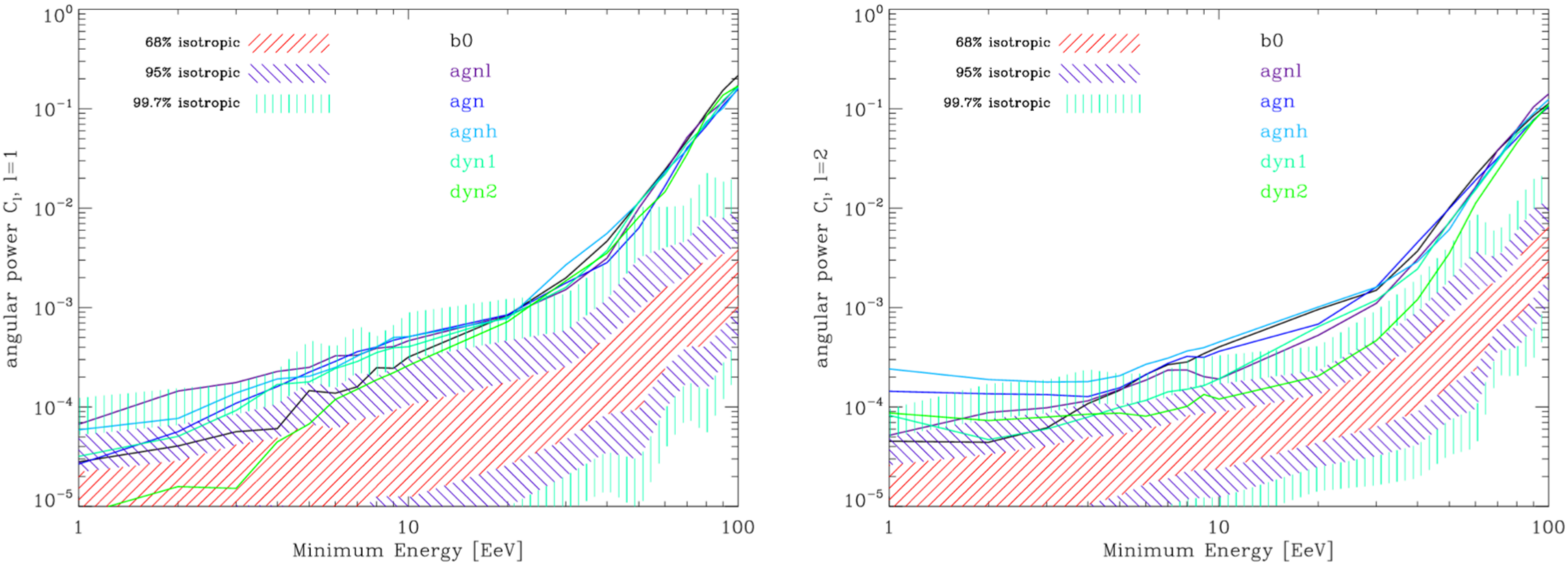

Figure 10. Angular power for the first two multipoles as function of minimum energy of UHECR events observed by ID61.

based on ENZO simulations

Hackstein, Vazza, Brüggen, Sigl, Dundovic,
Mon.Not.Roy.Astron.Soc. 462 (2016) no.4, 3660 [arXiv:1607.08872]

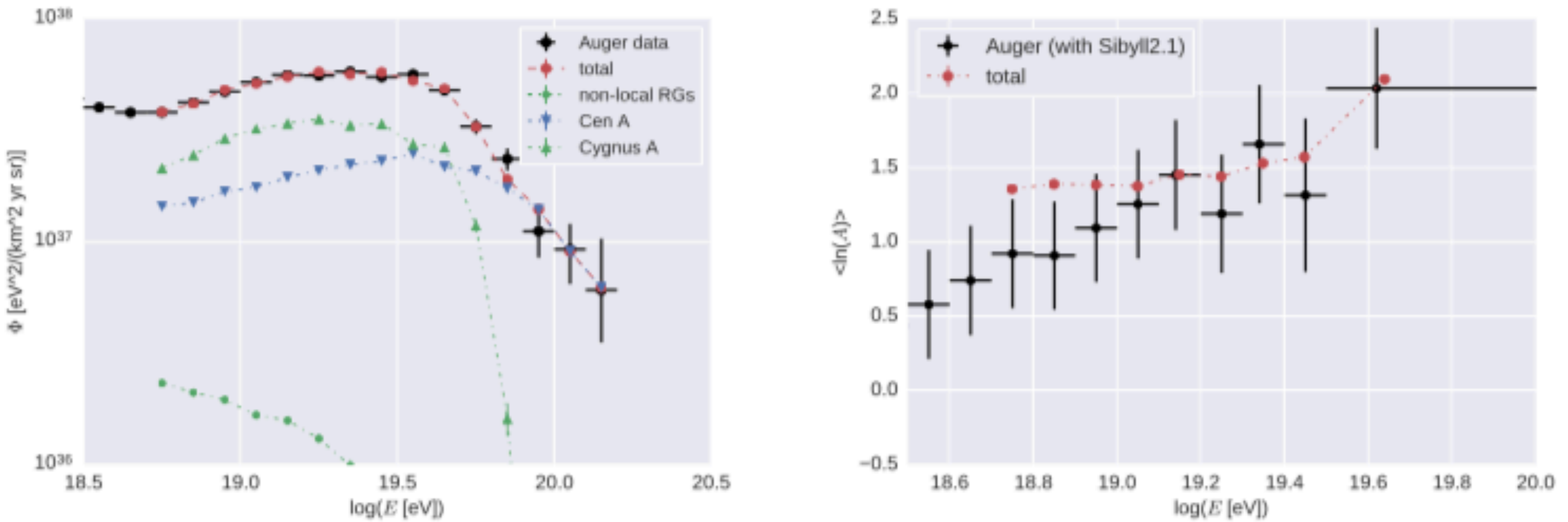

Figure 11. Best-fit results to energy spectrum (left) and chemical composition (right) using Sibyll2.1 and the heavy composition scenario with powerful Centaurus A.

based on a catalogue of radio galaxies where each source has individual injection parameters based on luminosity etc.

Eichmann et al., JCAP 1802 (2018) 036 [arXiv:1701.06792]

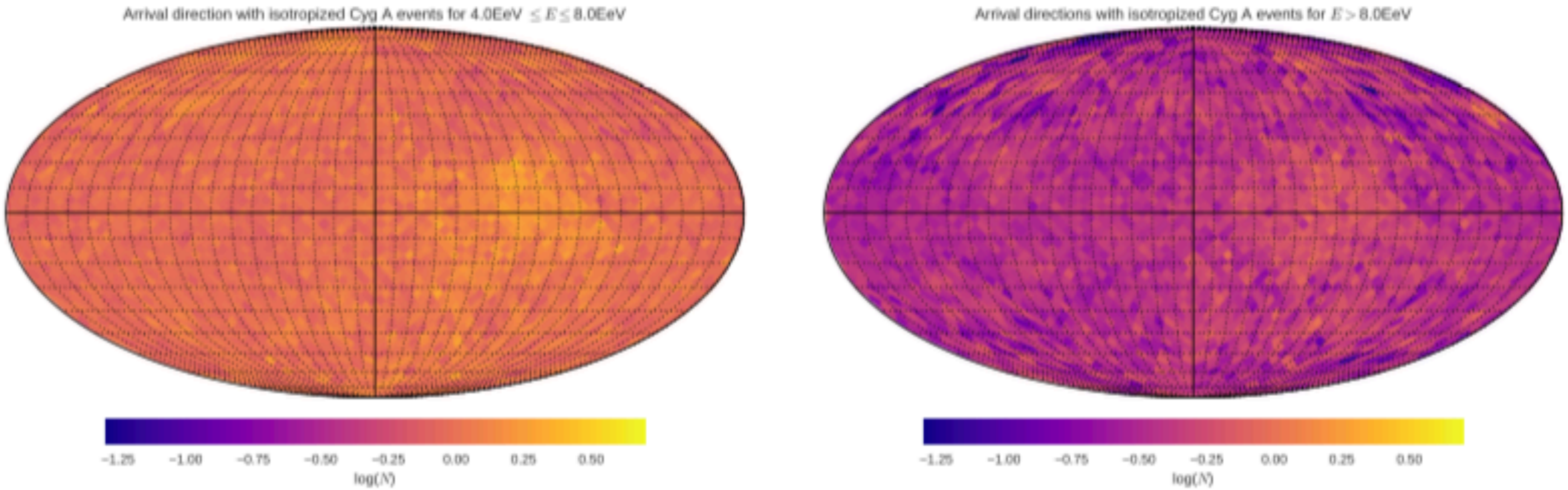

Figure 13. Skymap with isotropized Cygnus A events for $4\,\mathrm{EeV} \leq E \leq 8\,\mathrm{EeV}$ (left), and $E > 8\,\mathrm{EeV}$ (right) using Sibyll2.1 and the light composition scenario with a powerful Centaurus A.

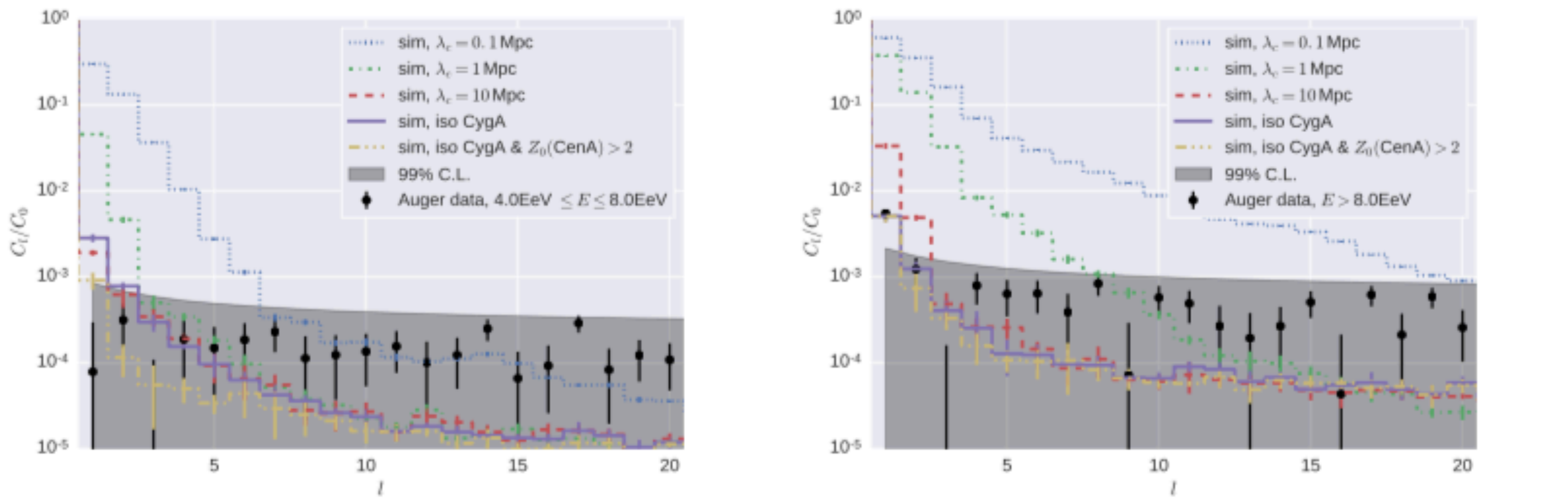

Figure 14. Angular power spectrum with isotropized (solid and dash-dotted line) and non-deflected (dashed line) Cygnus A events for $4\,\mathrm{EeV} \leq E \leq 8\,\mathrm{EeV}$ (left), and $E > 8\,\mathrm{EeV}$ (right) using Sibyll2.1 and the light composition scenario with a powerful Centaurus A.

Eichmann et al., JCAP 1802 (2018) 036 [arXiv:1701.06792]

Many other models have already provided predictions for multipoles/autocorrelations/correlations etc, e.g.

Kalashev, Pshirkov, Zotov, arXiv:1810.02284
Sigl, Miniati, Ensslin, PRD 70, 043007 (2004)

Conclusions

1.) A fraction ~ 10^{-3} of the total non-thermal power is sufficient to explain cosmic ray fluxes

2.) Maximal acceleration energy could be quite universal/not very source dependent

3.) Energy densities in cosmic rays, gamma-rays and neutrinos are all comparable -> “calorimetry”

4.) The observed X_{max} distribution and muon number and production depth in air showers provides potential constraints on hadronic interaction models: current models do not fully explain the data, however, systematic uncertainties are still significant.

5.) The sources of ultra-high energy cosmic rays are still not identified due to rather small anisotropies; composition seems to become heavier at the highest energies which appears economic in terms of shock acceleration power

6.) 3-dimensional modeling becomes more and more important